https://doi.org/10.1016/j.jsv.2019.02.042

Sound transmission through a grating of acoustic metamaterial under oblique sound incidence

Xiang Yu,[1)] Zhenbo Lu[2)], Tuo Liu,[3)] Li Cheng,[3)] Jie Zhu,[3)] and Fangsen Cui[1)*]

1) Institute of High Performance Computing, A*STAR, Singapore 138632

2) Temasek Laboratories, National University of Singapore, Singapore, 117411

3) Department of Mechanical Engineering, The Hong Kong Polytechnic University, Hong Kong 999077

*Corresponding author (F. Cui)

Institute of High Performance Computing, A*STAR, Singapore 138632.

Tel: 0065-64191334; Fax: 0065-64674350; Email: cuifs@ihpc.a-star.edu.sg

Abstract

This study investigates into the sound transmission through a baffled metamaterial grating under oblique sound incidence. The single-layer grating of acoustic metamaterial is constructed by periodically arranging sub-wavelength unit cells in a slab, which is embedded into a rigid baffle between two acoustic domains. The metamaterial unit cell consists of an open duct decorated with coiled resonators, which suppresses sound transmission near its acoustic stop-band. The space-coiling structure allows the metamaterial to operate at low frequency with a compact size. Analytical approach to calculate the sound transmission loss (STL) of the combined baffle is developed, which is then employed to study the transmission characteristics of the metamaterial grating under oblique sound incidence. The periodicity of the grating elements and the sound incidence angle significantly affect the STL. It is shown that both effects can be explained using an interference model based on an array of radiators. The STL behavior of the acoustic grating is governed by three main effects, including the stop-band behavior of the unit cell, the sound diffraction effect, and the interference relationship among the periodic unit cells. Detailed mechanism studies for these effects are discussed using numerical examples, and experimental validation is conducted to verify the proposed numerical approach. This study presents a theoretical framework to predict the performance of acoustic gratings comprised of metamaterial unit cells, which can be further extended to study acoustic metasurfaces with phase tailoring functionality.

Keywords: acoustic grating, sound insulation, sound transmission loss, acoustic interference, acoustic metamaterial.

1. Introduction

Acoustic metamaterials are a type of artificial materials that are designed to provide exotic properties absent in nature. The study of using acoustic metamaterials to manipulate sound wave propagation has received much attention, particularly for the purpose of low-frequency sound absorption and isolation beyond the restriction of dimension and weight [1-3]. For example, the initial realization by incorporating metal spheres in soft silicone epoxy exhibits negative dynamic mass induced by the resonance effect, which leads to strong sound wave attenuation [4]. The membrane-type acoustic metamaterial uses a simple and compact construction to realize a system with negative dynamic mass [5]. The metamaterial based on Helmholtz resonators demonstrates negative modulus which induces deep sub-wavelength sound isolation [6]. In contrast to the Bragg scattering sonic crystals whose lattice constant is usually on the order of half wavelength [7], the idea of metamaterials is to take the advantage of locally resonant systems to control sound wave on a sub-wavelength scale. This could potentially overcome the limitation of bulky structures for noise control in audible frequency regime and could substantially innovates novel acoustic applications.

Several types of locally resonant systems can be used as the basic unit cell of an acoustic metamaterial. For example, the membrane-type metamaterial uses a concentrated mass attached onto a membrane to behave like a spring-mass-damper system, thus generating sub-wavelength sound transmission [8-10] and absorption [11]. The periodic Helmholtz resonator array isolates sound at ultra-low frequency

range by using the transmittance stop-band generated by local resonance [6]. The Mie-resonator [12] and split tube resonator [13] can be viewed as variations of Helmholtz resonator and showed significant sub-wavelength feature. These examples demonstrate the deep sub-wavelength property of metamaterial with extremely compact geometry, but practical sound control is often preferable over a broadband of frequencies, being incompatible with the resonance-based metamaterials. This calls for a balance between the sub-wavelength property and the broadband performance.

Acoustic metasurfaces are newer class of acoustic metamaterials which have surface profile and sub-wavelength thickness, allowing on-demand tailoring of sound propagation by imposing a specific boundary. The study in this category starts with an attempt to arbitrarily steer transmitted or reflected wavefront by introducing phase shifts to the incident waves [14, 15]. The wavefront modulation is a diffractive phenomenon governed by phase control, and later on the metasurface is broadened to the traditional categories of sound absorption [11, 16], where the constituting unit cells can be identical without possessing phase difference. An attempt to realize an ultra-sparse metasurface for both sound isolation and air ventilation was made by using artificial Mie resonators [12], but the demonstrated insertion loss was low due to the low filling ratio.

The class of metamaterial unit with an acoustic duct can be utilized for both sound reduction and ventilation. The duct allows natural air passage while the resonators attached to its side-branch can provide attenuation effect on sound transmission. For example, a two-dimensional array of low loss cylindrical cavities

was studied, showing negative bulk modulus and dispersion relation of acoustic bands [17]. The resonant tubular array demonstrated continuous tuning of compressibility in a wide range [18]. A sub-wavelength acoustic panel based on resonant ducts was constructed to provide high sound absorption using accumulation of resonances [19, 20]. Conceptually, the ensemble of duct and attached resonators can be considered as a metamaterial unit cell. If we periodically arrange such metamaterial unit cells in a slab, an acoustic grating can be constructed to realize special acoustic functions by making use of the unusual property of the unit cells and also the interaction among unit cells. As the thickness of a single-layer acoustic grating equals to that of the constituting element, the slab structure can possess excellent geometric advantage benefiting from the sub-wavelength size of the unit cells.

This study investigates the sound transmission characteristics in a single-layer acoustic grating formed by periodic arrangement of duct-like metamaterial unit cells. The metamaterial unit cell comprises a short acoustic duct decorated with an array of coiled resonators in the side-branch, forming a duct-like metamaterial which allows for both sound isolation and air ventilation. The metamaterial grating is embedded in an infinite baffle between two acoustic domains. We introduce a hybrid numerical model to predict the sound transmission behavior of the system, where analytical method is used to model the incident and transmitted sound fields, and finite element method is used to model the metamaterial with complicated geometry. The proposed approach provides an accurate and effective tool to study the involved parameters and to uncover the physical aspects.

This paper is organized as follows: Sec. 2 describes a numerical approach which is specifically developed to model a baffled acoustic slab composed of metamaterial grating elements. The acoustic fields on both sides of the baffle are modeled analytically, and the connections via grating elements are modeled as waveguides using the transfer matrix parameters. In Sec. 3, the one-dimensional acoustic transmission through a unit cell is first studied using a simplified impedance tube model. It is shown that the unit cell formed by a duct decorated with coiled resonators is a type of metamaterial possessing resonance-induced negative modulus. Its effective material property and layer effect is analyzed. Using the proposed numerical approach, Sec. 4 further analyzes the STL of the acoustic grating. Particular attentions are paid to uncovering the effect of unit cell periodicity and sound incidence angle. Experimental test to validate the simulation result and proposed numerical framework is presented in Sec. 5.

2. Numerical approach

Let us consider a two-dimensional acoustic slab comprised of a number of metamaterial unit cells arranged periodically, forming a single-layer grating as shown in Fig. 1(a). The metamaterial unit cells are open acoustic ducts decorated with coiled resonators, as sketched in Fig. 1(b), the space-coiling structure is to enhance the low frequency sound attenuation performance. The whole slab is assumed to be embedded in an infinite baffle. The boundaries of the unit cells and the separation between

grating elements are assumed as rigid. Using the Cartesian coordinate system, let *x*-axis denote the slab normal and *y*-axis the slab tangential. The sound incidence angle α is defined relative to the slab normal, with $\alpha = 0^\circ$ being normal incidence case and the $\alpha = 90^\circ$ being the grazing incidence case.

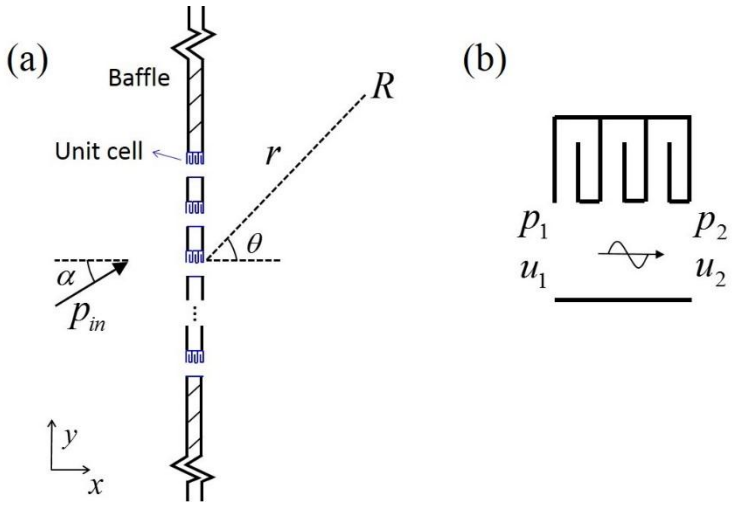

Fig. 1. (a) A slab comprised of metamaterial unit cells arranged periodically to form a single-layer acoustic grating. Oblique sound incidence angle is defined relative to the slab normal; (b) The metamaterial unit cell is an open duct decorated with coiled resonators.

Assuming the system is excited by plane wave with oblique incidence angle α, the incident sound pressure field on the left hand side of the baffle can be expressed as [21]:

$$p_{in}(x, y, \omega) = p_0 e^{j(\omega t - kx\cos\alpha - ky\sin\alpha)} \tag{1}$$

where p_{in} is the incident pressure field, p_0 is the amplitude of incident wave; $j = \sqrt{-1}$; k is the wave number $k = \omega / c_0 = 2\pi f / c_0$, ω is the angular frequency and c_0 is the speed of sound in air. At the slab interface where *x*=0, the above expression

reduces to $p_0 e^{j(\omega t - ky\sin\alpha)}$. The time dependence $e^{j\omega t}$ can be neglected if we assume harmonic analysis.

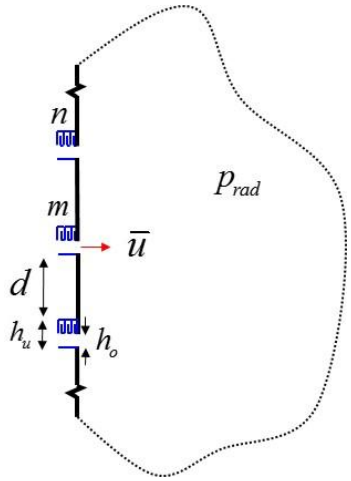

Fig. 2. Sound radiation from unit cell apertures into a semi-infinite free space.

On the right hand side of the slab, the transmitted sound through the unit cell causes an air velocity disturbance at the outlet aperture and radiates into the receiving field. Under the baffled condition, sound radiation from the periodic outlet apertures can be modeled as cylindrical waves radiating into a semi-infinite free space, as illustrated in Fig. 2. To determine the radiation impedance between the radiated pressure field and the unit cell velocity, the governing Helmholtz equation is:

$$[\nabla^2 + k^2(\vec{r})]p_{rad}(\vec{r},\omega) = 0 \tag{2}$$

where p_{rad} is the radiated sound pressure, ∇ is the Laplacian operator, $\nabla^2 = \frac{\partial^2}{\partial x^2} + \frac{\partial^2}{\partial y^2}$ for Cartesian coordinate system and $\nabla^2 = \frac{1}{r}\frac{\partial}{\partial r} r \frac{\partial}{\partial r}$ for cylindrical coordinate system, $\vec{r}$ is the position vector of receiving point *R*. By omitting the time-dependent term $e^{j\omega t}$, the solution to the above equation is:

$$p_{rad}(\vec{r}) = aH_0^{(2)}(kr) \tag{3}$$

where *a* is the amplitude determined by the strength of sound radiation source, $H_0^{(2)}$ is the zero order Hankel of the second kind.

Assuming the outlet aperture of a unit cell is small compared to the acoustic wavelength, and the receiving point *R* is located in the far field, the outlet aperture can be approximated as a point source with uniform velocity. The radiation strength is $a = k\rho_0 c_0 q/2$ and Eq. (3) can be further written as [22]:

$$p_{rad}(\vec{r}) = \frac{k\rho_0 c_0 q}{2} H_0^{(2)}(kr) \tag{4}$$

where *q* is to describe strength of air velocity disturbance at the outlet aperture: $\mathrm{d}q = \bar{u}\mathrm{d}y$, with d here being the differential operator, $\bar{u}$ being the normal air velocity averaged over the aperture area h_o.

Assuming the radiated sound pressure field in the receiving side is a linear superposition of the sound fields generated by all the periodic unit cells. The sound pressure p_n at a specific unit cell *n* due to excitation from all the unit cells including cell *n* itself, inversely affects the pressure continuity relation. This coupling effect has to be taken into account to solve the coupled system response. The mutual radiation impedance between a receiving unit cell *n* and an exciting unit cell *m* is $Z_{nm} = p_n / \bar{u}_m$, and the self-radiation impedance is $Z_{mm} = p_m / \bar{u}_m$. By translating the origin of the coordinate system to the center of the outlet aperture at the exciting cell *m*, i.e., *y*=0, the acoustic pressure on the receiving cell *n* due to an exciting cell *m*, provided that $m \neq n$ is:

$$p_n(y_n) = \frac{k\rho_0 c_0}{2} \int_{-h_o/2}^{h_o/2} \bar{u}_m H_0^{(2)}(ky) dy \tag{5}$$

where the integration is taken over the radiating outlet aperture at cell *m* from $-h_o/2$ to $h_o/2$. The mutual radiation impedance between cell *m* and *n* is thus:

$$Z_{nm} = \frac{p_n}{\bar{u}_m} = \frac{k\rho_0 c_0 h_o}{2} H_0^{(2)}(kd_{nm}) \tag{6}$$

where d_{nm} is the separation distance between the cell *n* and *m*.

For the self-radiation impedance where $m = n$:

$$Z_{mm} = \frac{p_m}{\bar{u}_m} = \frac{k\rho_0 c_0}{2} \int_{-h_0/2}^{h_0/2} H_0^{(2)}(ky) dy \tag{7}$$

It is worth noting that for three-dimensional case, Eq. (6) and (7) can be rewritten using the well-known Rayleigh's integral. As a numerical example, the calculated radiation impedance, including real and imaginary parts of the self and mutual impedance, are plotted in Fig. 3. The size of the aperture h_o is 0.12 m and the distance d_{nm} is also 0.12 m.

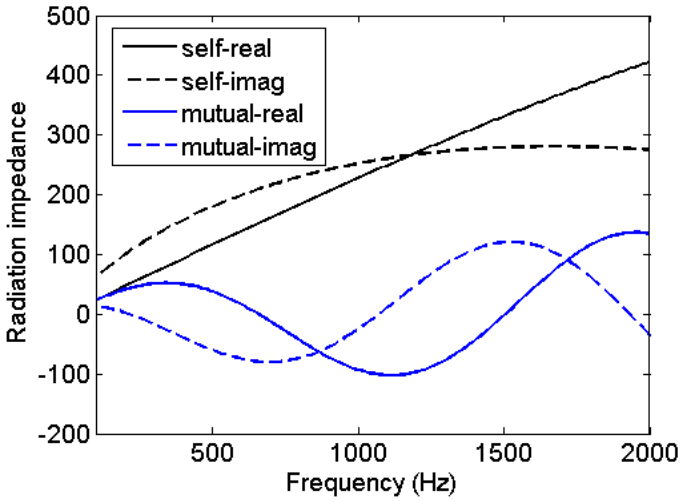

Fig. 3. The real and imaginary part of self and mutual radiation impedance, aperture size h_o is 0.12 m, distance d_{nm} is 0.12 m.

The metamaterial unit cell is modeled using a numerical approach to connect the incident and receiving sound fields analytically described as above. The sub-wavelength property of the unit cell makes it reasonable to consider its interaction with the adjacent acoustic fields as a one-dimensional waveguide. The cascaded coiled resonators in the side-branch generates accumulated effect on the sound transmission when sound propagates through a unit cell. For the metamaterial unit cell as shown in Fig. 1(b), its acoustic wave propagation in the duct is one-dimensional if the frequency range is below the cut-off frequency determined by the aperture size: $f_c = c_0 / 2h_o$. The one-dimensional waveguide can be described by the four-pole transfer matrix, which relates the pressure and velocity conditions on both ends of a unit cell as:

$$\begin{bmatrix} p_1 \\ u_1 \end{bmatrix} = \begin{bmatrix} A & B \\ C & D \end{bmatrix} \begin{bmatrix} p_2 \\ u_2 \end{bmatrix} \tag{8}$$

The four-pole parameters can be obtained either analytically or numerically, depending on the complexity of the unit cell geometry. To use numerical method such as Finite Element Method (FEM), the conditions to be imposed at the unit cell boundaries and the parameters can be obtained are:

$$\begin{aligned} u_2 = 0: & \begin{matrix} A = p_1 / p_2 \\ B = u_1 / p_2 \end{matrix} \\ p_2 = 0: & \begin{matrix} C = p_1 / u_2 \\ D = u_1 / u_2 \end{matrix} \end{aligned} \tag{9}$$

For a slab of acoustic grating composed of N periodic unit cells, the four-pole parameters for the identical unit cells are the same. At each unit cell, the sound pressure field on the incident side is a combination of the incident waves $\mathbf{p_{in}}$ and the reflected waves $\mathbf{Z}_r\mathbf{u_1}$, where $\mathbf{p_{in}}$ and $\mathbf{u_1}$ are $N\times 1$ vectors containing p_{in} and u_1 for each unit cell, $\mathbf{Z}_r$ is a $N\times N$ matrix containing the mutual- and self-radiation impedances calculated using Eq. (6)&(7). The transmitted sound field on the receiving side is $\mathbf{Z}_r\mathbf{u_2}$. Note that the radiation impedance $\mathbf{Z}_r$ for the reflected and transmitted sound fields are the same for the baffled condition assumed here. With the pressure continuity conditions, the coupled system can be written as [23]:

$$\begin{aligned}\mathbf{p_{in}}-\mathbf{Z}_r\mathbf{u_1}&=\mathbf{p_1}\\ \mathbf{Z}_r\mathbf{u_2}&=\mathbf{p_2}\end{aligned} \tag{10}$$

Together with the four-pole matrix relation for all the unit cells in Eq. (8), the entire system can be described by:

$$\begin{bmatrix}\mathbf{A} & \mathbf{B} & \mathbf{Z}_r\\ \mathbf{C} & \mathbf{D} & -\mathbf{I}\\ -\mathbf{I} & \mathbf{Z}_r & \mathbf{0}\end{bmatrix}\begin{bmatrix}\mathbf{p_2}\\ \mathbf{u_2}\\ \mathbf{u_1}\end{bmatrix}=\begin{bmatrix}\mathbf{p_{in}}\\ \mathbf{0}\\ \mathbf{0}\end{bmatrix} \tag{11}$$

The system response can be solved once $\mathbf{u_1}$ and $\mathbf{u}_2$ are obtained. To calculate the STL, the sound power impinging on the slab is:

$$W_{in}=\frac{|p_0|^2}{2\rho_0 c_0}S_{slab}\cos\alpha \tag{12}$$

where S_{slab} is the total area of the slab. The transmitted sound power from the slab is:

$$W_{trans}=\frac{1}{2}\int \mathrm{Re}(p_{rad}\cdot\bar{u}^*)dy=\frac{1}{2}\sum_1^N \mathrm{Re}[(\mathbf{Z}_r\cdot\mathbf{u_2})\cdot\mathbf{u_2}^*]h_0 \tag{13}$$

where asterisk denotes the complex conjugate of the air velocity at the outlet aperture.

The STL of the acoustic grating under baffled condition is finally obtained as:

$$\mathrm{STL} = 10\log_{10}(W_{in} / W_{trans}) \tag{14}$$

3. One-dimensional acoustic transmission through a unit cell

We first analyze the acoustic transmission characteristics in a metamaterial unit cell and its effective material properties using a simplified one-dimensional condition. As shown in Fig. 4, the unit cell (with only one resonator layer) is placed in an acoustic duct whose height is identical to the unit cell height. The reflection and transmission relationship is studied in an impedance tube model to obtain the intrinsic property of the unit cell itself. Dimensions of the unit cell are as sketched in Fig. 4. The unit cell height is 0.12 m, aperture height is 0.06 m, and the thickness for one resonator layer is 0.04 m. The space-coiling resonator results in two parallel sub-chambers with identical width of 0.018 m. The thickness of all boundary walls is set as 0.002 m. Plane wave sound incidence is applied at the duct left end and travels towards the unit cell. Anechoic termination is applied at the right end outlet assuming no reflections. The interior acoustic boundaries are assumed as rigid thus the system is lossless. A standard retrieval method is followed to extract the effective material properties from the reflection and transmission coefficient of the unit cell [24]. The impedance of the material Z is calculated as:

$$Z = \frac{\mp\sqrt{(R^2 - T^2 - 1)^2 - 4T^2}}{1 - 2R + R^2 - T^2} \tag{15}$$

where R and T are the complex reflection and transmission coefficients containing the phase information. To obtain R and T, a standard impedance tube FEM model is employed to analyze the unit cell as shown in Fig. 4 [23]. The refraction index ξ can be calculated as:

$$\xi = \frac{-j\log[(1-R^2+T^2 \mp \sqrt{(R^2-T^2-1)^2-4T^2})/2T]+2\pi M}{kL} \tag{16}$$

where L is the width of the unit cell and M is the branch number. A minimum thickness metamaterial that corresponds to $M = 0$ is used during the retrieval process, which has been proved to produce the best result [24, 25]. The effective bulk modulus of the material and the effective mass density can then be obtained as:

$$\begin{aligned} \kappa_{eff} &= Z/\xi \\ \rho_{eff} &= Z\xi \end{aligned} \tag{17}$$

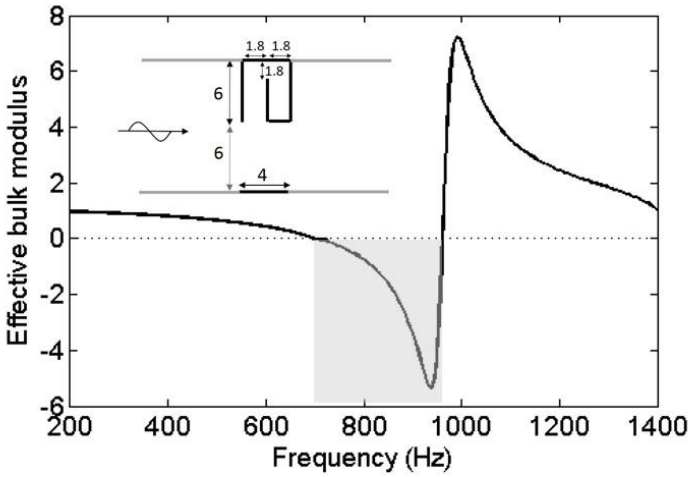

Fig. 4. The effective bulk modulus calculated for a single unit cell with single coiled resonator layer, dimensions are given in cm.

In Fig. 4, the obtained effective bulk modulus κ_{eff} is plotted, which shows a region with negative parameter values. The negative feature arises from the local

resonance of the coiled resonator, which occurs in the vicinity of the resonant frequency in character. Due to the coupling between resonator's opening at the neck area with the longitudinal wave propagation in the duct, the negative value frequency is broadened to a frequency range (700-950 Hz). The resonator can be further coiled to obtain deeper sub-wavelength effect, but this could impose a significant impedance mismatch and negatively affect the attenuation bandwidth provided by the attached resonator. Hence, the side-branch resonator is only folded once here.

Along the wave propagation direction, additional resonator layers can be added to broaden the attenuation bandwidth. Although ideally, infinite layers of identical resonators can be combined to generate complete acoustic stop-band, practically, only limited resonator layers are allowed and the resulted acoustic grating is preferable to be thinner. In Fig. 5, the transmittance characteristics of a unit cell with different resonator layers are plotted. From one to four layers, the frequencies where the transmittance dip occurs generally remain the same, meaning the inherent effective property of the metamaterial is unchanged. The attenuation bandwidth with low transmittance is however enlarged with more layers. To effectively block sound transmission, we generally consider a transmittance lower than 0.2 to be adequate. Therefore three resonator layers are chosen for a unit cell, as further increase the layers does not show substantial effect. The resulted outer dimension of a unit cell is 0.12 m by 0.12 m.

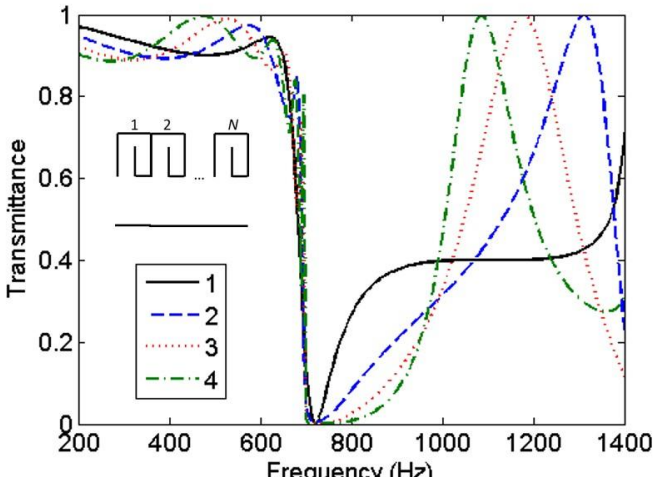

Fig. 5. Transmittance of a unit cell with multiple layers of coiled resonators.

The final unit cell geometry is sketched in Fig. 6(a), and the one-dimensional STL of the unit cell with duct termination on both ends is shown in Fig. 6(b). The STL curve shows a dominant peak at 700 - 900 Hz with attenuation over 5 dB. The size of the unit cell (both height and thickness equal to 0.12 m) is about 0.27 of the acoustic wavelength at the main working frequency near 780 Hz, i.e., 0.27 λ , demonstrating a sub-wavelength character. The four-pole parameters of the unit cell obtained using Eq. (9) are presented in Fig. 7.

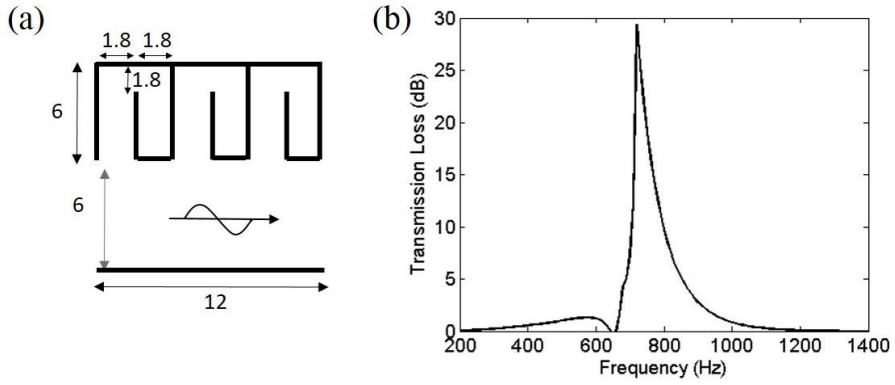

Fig. 6. (a) Unit cell geometry with three coiled resonators (in cm) and (b) the one-dimensional sound transmission loss.

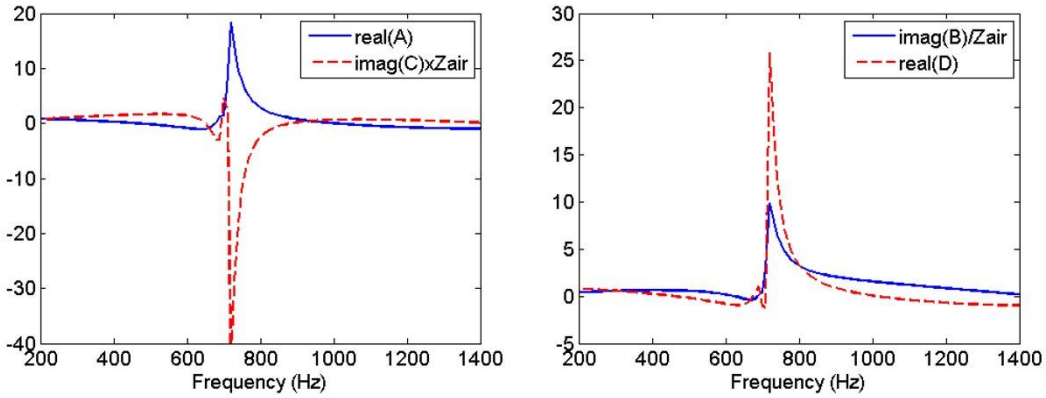

Fig. 7. The four-pole parameters of the unit cell obtained using Eq. (9).

4. Numerical examples

4.1 Single unit cell

The STL of a single metamaterial unit cell on an infinite baffle is first investigated. Fig. 8 presents the STL calculated using the numerical approach introduced in Sec. 2. The STL results are compared for three sound incidence angles: normal $\alpha = 0^{\circ}$, oblique $\alpha = 45^{\circ}$ and $\alpha = 60^{\circ}$, respectively. Generally, comparing to the duct-terminated unit cell STL in Fig. 6(b), the baffled STL shows more variations along the frequency range. The STL peak occurs at the same frequency of 780 Hz due to the stop-band behavior of the unit cell, which is as expected. An obvious drop in the STL curve appears at 500 Hz for all three incidence angles, where the STL could reach negative values. This was not found in the duct-terminated case.

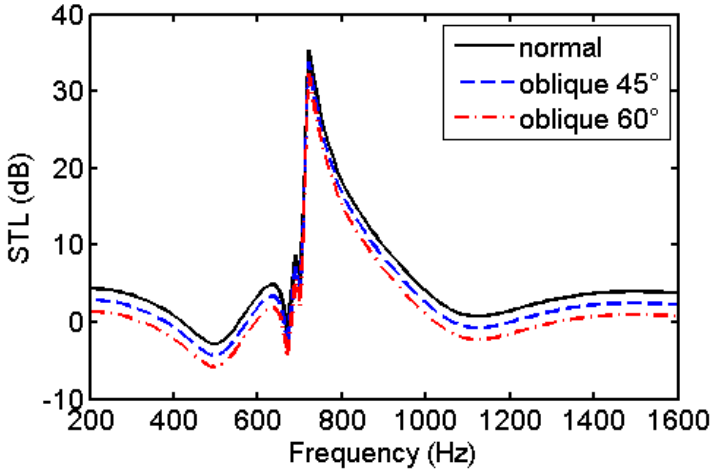

Fig. 8. STL of a single unit cell under normal or oblique sound incidence.

As the sound fields on both sides of the unit cell are now semi-infinite, the negative STL can be explained by the sound diffraction effect. When the wavelength is longer than the size of the unit cell aperture and when the frequency of interest is below the stop-band (around 780 Hz), the unit cell can be viewed as an open acoustic duct connecting the two acoustic fields [26, 27]. At the transmission maxima due to resonance effect of the duct-like aperture, the transmission coefficient can be greater than unity and thus the STL can yield negative value, which is an artificial effect due to the STL definition in Eq. (14). To qualitatively explain this, the sound pressure field and intensity flow through the unit cell (represented by streamlines) are plotted at 500 Hz in Fig. 9, corresponding to the first dip in the STL curve in Fig. 8. Sound diffraction pattern in the incident field can be clearly observed, where sound squeezes into the aperture and the intensity flow is diffracted at the aperture edge. This results in more sound energy entering and transmitting through the aperture from the neighborhood, making the calculation of W_{trans} greater than W_{in}.

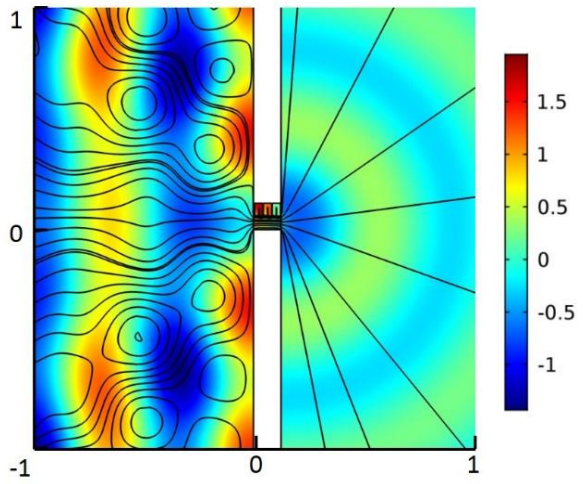

Fig. 9. Sound pressure field and intensity flow (represented by streamlines) at 500 Hz. Sound diffraction pattern in the incident field can be observed.

To quantify the diffraction effect numerically, the transmission of a duct-like aperture of size h_0 and thickness L can be calculated using the following four-pore parameters:

$$\begin{bmatrix} p_1 \\ u_1 \end{bmatrix} = \begin{bmatrix} \cos(kL) & j\sin(kL)\rho_0 c_0 \\ j\sin(kL)/\rho_0 c_0 & \sin(kL) \end{bmatrix} \begin{bmatrix} p_2 \\ u_2 \end{bmatrix}. \tag{18}$$

For a duct-like aperture of size h_o=0.06 m and thickness L=0.12 m, the calculated straight duct STL is plotted in Fig. 10. The predicted STL dip at 850 Hz however does not match with the metamaterial STL dip at 500 Hz. By examining the phase transition at the entrance of the metamaterial block in the pressure plot (Fig. 9), the coiling space in the resonator effectively elongate the characteristic duct thickness as illustrated in Fig. 10. After taking into account the coiled path and using an elongated effective thickness of L=0.24 m, the STL of a duct-like aperture is calculated, whose first two resonant dips (500 Hz and 1150 Hz) match well with the metamaterial STL.

This indicates the major difference in the unit cell STL between one-dimensional condition (Fig. 6) and baffled condition (Fig. 8) is due to sound diffraction effect.

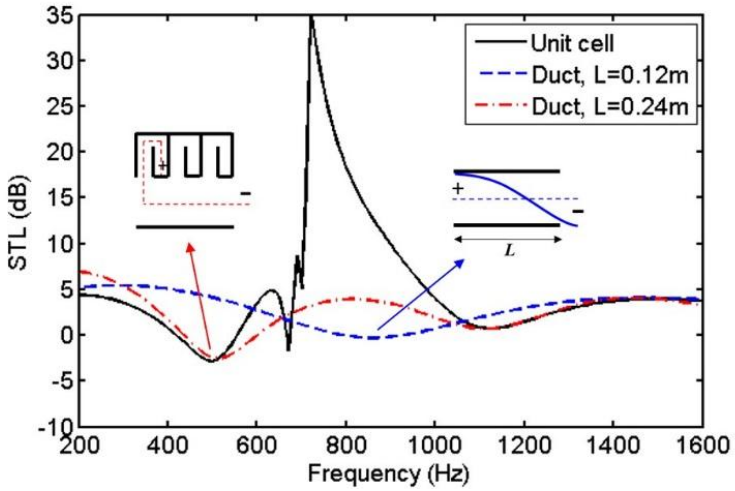

Fig. 10. The STL dips at 500 Hz and 1150 Hz match with the diffraction behavior in the sound transmission through a duct-like aperture.

For the oblique incidence cases $\alpha = 45^{\circ}$ and 60°, the STL curve is shifted lower simply because the incident sound intensity in Eq. (12) involves a factor of $\cos\alpha$. The curve shape is unchanged because the unit cell reacts locally as a one-dimensional waveguide. This assumption remains valid until the cut-off frequency is reached when $f_c = 343/0.06 = 5700$ Hz, which is much higher than the frequency of interest here. Generally, the metamaterial unit cell provides high sound insulation effect near its stop-band frequency as determined in Sec. 3, where the STL peak can exceed 30 dB in prediction. The single unit cell STL under baffled condition is also dependent on the sound incidence angle.

4.2 Metamaterial grating under normal sound incidence

The STL of an acoustic grating comprising five identical unit cells is investigated in this section, where the periodicity can vary with a different separation distance *d*. With five unit cells and d = 0 m, i.e., the unit cells are closely adjacent to each other, Fig. 11 shows the grating's STL is more flattened compared to the single unit cell STL. The 5 cells STL does not show diffraction induced resonance pattern, and is closer to the one-dimensional duct-terminated STL in Fig. 6. This is because the diffraction effect becomes less obvious as the filling ratio of grating elements increases. When the separation distance increases to d = 0.12 m, the diffraction induced STL dips appear again, and slightly move to a higher frequency (around 550 Hz) comparing to the single cell STL. Interestingly, a new STL dome rises from 1300 Hz to 1500 Hz when the 5 cells are separated by d= 0.12 m. This was not found in the previous two cases with single unit cell or tightly joint unit cells.

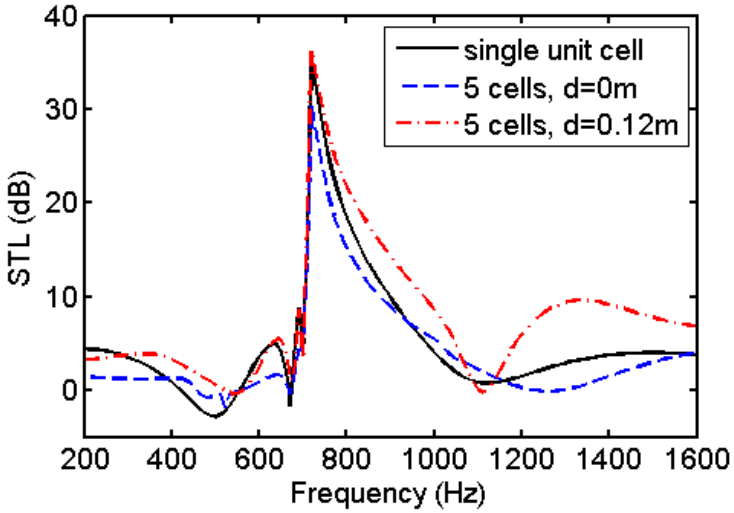

Fig. 11. STL of an acoustic grating composed of five unit cells, with different separation distance, d = 0 m and d = 0.12 m.

The formation of the new high STL region can be explained by the radiation inference among the periodic unit cells. To explain this, a theoretical sound radiation model is illustrated in Fig. 12, where the outlet apertures of the periodic grating elements are simplified as an array of point radiators. The separation distance between two radiators, denoted as one period *b*, is $b = d + h_u$, with h_u being the unit cell size. For each single radiator, the radiated sound pressure at a receiving point *R* is:

$$p(\omega, r) = \frac{a}{\sqrt{r}} e^{(j\omega t - kr)} \tag{19}$$

where *r* is the separation distance between the source radiator and the receiving point. *a* is the pressure amplitude determined by the strength of sound source.

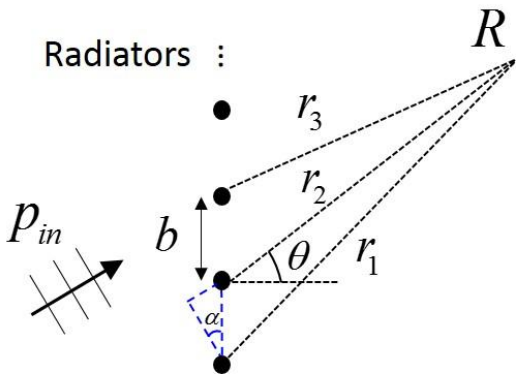

Fig. 12. The aperture outlets of the periodic grating elements are simplified as an array of point radiators to explain the radiation interference effect.

Assuming the receiving point is in the far field, the distance relative to the radiators can be approximated by:

$$\begin{aligned} r_2 &= r_1 + b\sin\theta \\ &\cdots \\ r_N &= r_1 + (N-1)b\sin\theta \end{aligned} \tag{20}$$

The sound pressure at the receiver point *R* as a result of the super-positioned sound field due to an array of radiators is:

$$\begin{aligned} p(\theta,\omega,r) &= \frac{a}{\sqrt{r}} e^{(j\omega t - kr_1)}[1 + e^{-jkb\sin\theta} + \cdots + e^{-jk(N-1)b\sin\theta}] \\ &= \frac{a}{\sqrt{r}} e^{(j\omega t - kr_1)} \left[\frac{1 - e^{-jNkb\sin\theta}}{1 - e^{-jkb\sin\theta}} \right] \\ &= \frac{a}{\sqrt{r}} e^{(j\omega t - kr_1)} e^{-jNkb\sin\theta/2} e^{jkb\sin\theta/2} \left[\frac{e^{jNkb\sin\theta/2} - e^{-jNkb\sin\theta/2}}{e^{jkb\sin\theta/2} - e^{-jkb\sin\theta/2}} \right] \\ &\approx \frac{a}{\sqrt{r}} e^{(j\omega t - kr)} \frac{\sin(Nkb\sin\theta/2)}{\sin(kb\sin\theta/2)} \end{aligned} \tag{21}$$

To determine the sound radiation pattern, the source strength term *a* can be normalized. The directivity pattern can then be derived from Eq. (21):

$$D(\theta,\omega) = \frac{p(\theta,\omega)}{p(0,\omega)} = \left| \frac{\sin(Nkb\sin\theta/2)}{N\sin(kb\sin\theta/2)} \right| \tag{22}$$

where $D(\theta,\omega)$ describes the strength of sound radiation in a specific angle θ relative to the normal angle $p(0,\omega)$. $D(\theta,\omega)$ in Eq. (22) is a function of the grating periodicity *N* and *b*, frequency *k* and radiation angle θ.

The radiated sound power to the far field is:

$$W(\omega) = \int_{\frac{-\pi}{2}}^{\frac{\pi}{2}} N^2 D(\theta,\omega)^2 d\theta = \int_{\frac{-\pi}{2}}^{\frac{\pi}{2}} \left| \frac{\sin(Nkb\sin\theta/2)}{\sin(kb\sin\theta/2)} \right|^2 d\theta \tag{23}$$

Using the expression in Eq. (23), the sound radiation intensity (power normalized by surface) in dB scale with unit cell distance *d*=0 m, 0.15 m, and 0.3 m are plotted in Fig. 13. With unit cell size h_u =0.12 m, the corresponding radiator distance are *b*=0.12 m, 0.27 m, and 0.42 m, respectively. For *d*=0 m, the radiated intensity is a continuously descending line. When *d* is increased to 0.15 m, the

intensity curve shows one trough induced by radiation interference at 1100 Hz. And *d*=0.3 m shows two troughs at 650 Hz and 1500 Hz, respectively. Comparing to the baseline curve with *d*=0 m, the interference effect among periodic unit cells could significantly affect the energy transmission, as the sound radiation intensity can differ 、more than 5 dB for different separation cases. In Fig. 14, the STLs of the acoustic grating (comprising 5 unit cells) with the three separation distances are illustrated. The frequencies where STL curve rises (marked by arrows) correlate well with those valleys in the intensity curve in Fig. 13, and the interference induced radiation deficiencies are transferred to those increments in the STL curve. This demonstrates the interference relationship in the periodic acoustic grating and its effect on sound transmission.

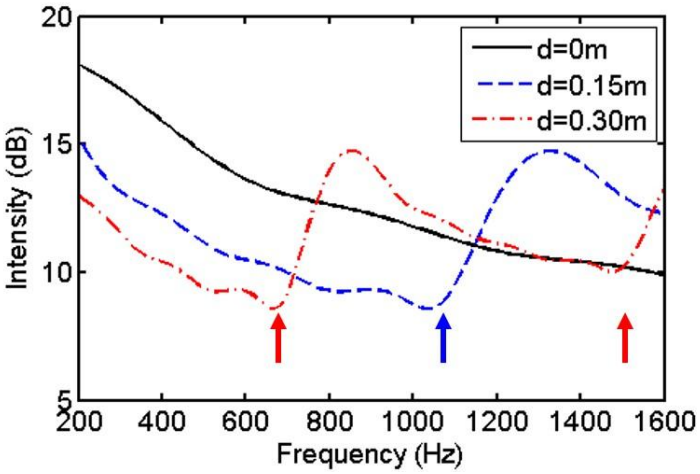

Fig. 13. Sound radiation intensity of five radiators separated by different distances. Arrows denote radiation valley due to destructive interference.

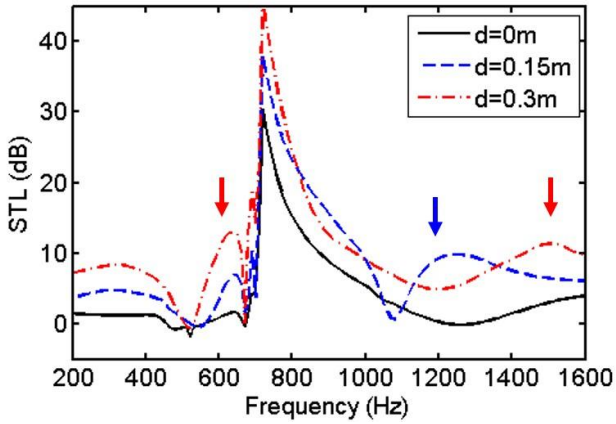

Fig. 14. STLs of acoustic grating comprising 5 unit cells with different separation distance *d*.

Equation (22) can be applied to determine the directivity of the transmitted sound through the acoustic grating. For illustration purpose, the directivity pattern for the case with d = 0.3 m is calculated at 650 Hz and 1500 Hz, corresponding to the two troughs in the radiation power curve. Figure 15 (left) shows the directivity polar plot at 650 Hz, where the main radiation direction is normal to the slab. The sound pressure distribution in the areas surrounding the acoustic grating is calculated and displayed on the right, which matches with the directivity obtained analytically using Eq. (22). Note that the polar plot only considers the radiation part (simplified using radiators), whereas the sound pressure distribution shows the fully coupled system response. At the second trough at 1500 Hz, directivity polar plot in Fig. 16 shows that the radiated sound field is scattered and indicates three distinct radiation angles. The sound pressure distribution plot of the coupled system again follows the simplified radiator model.

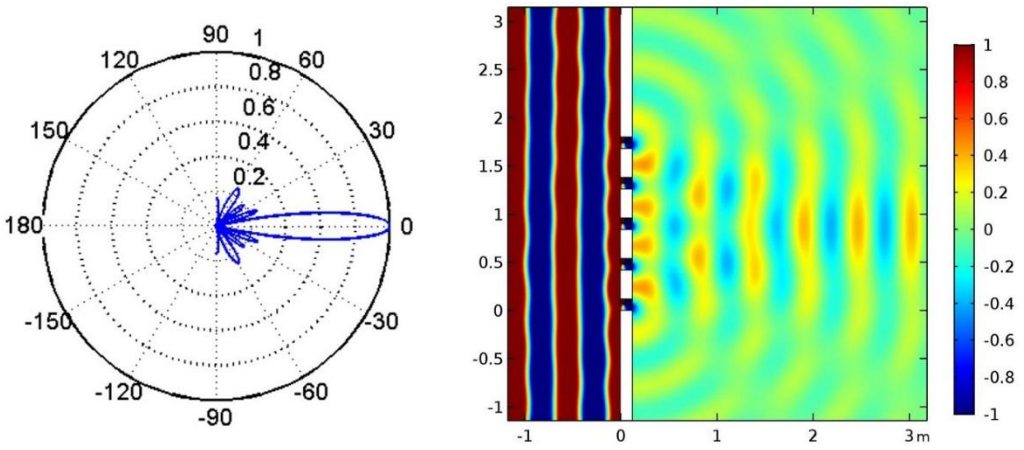

Fig. 15. The radiation directivity predicted using Eq. (22) (polar plot) and the sound pressure distribution in the coupled system at 650 Hz, d=0.3m, normal incidence.

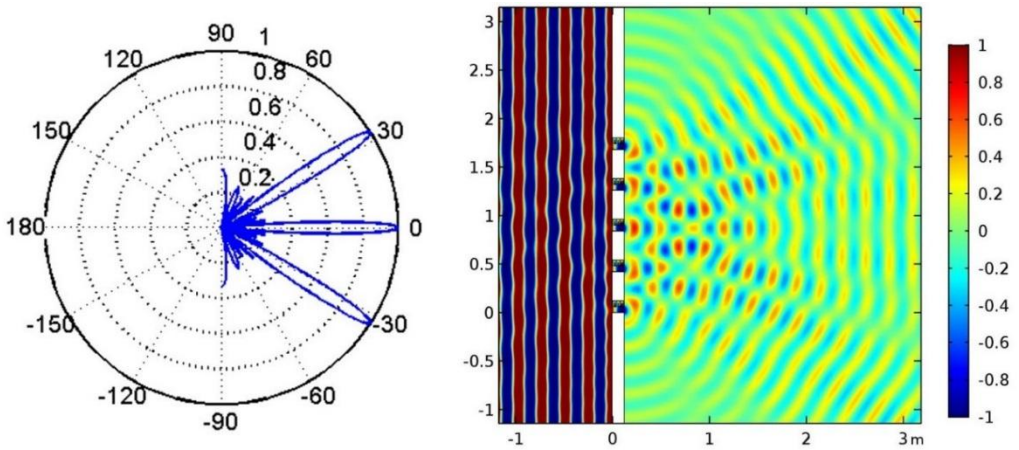

Fig. 16. The radiation directivity predicted using Eq. (22) (polar plot) and the sound pressure distribution in the coupled system at 1500 Hz, d=0.3 m, normal incidence.

4.3 Metamaterial grating under oblique sound incidence

When the sound incidence is oblique in an angle α relative to the slab normal, the grating elements in the acoustic slab involve extra phase difference term, which

could further change the sound radiation characteristics. The phase difference can be equivalently described using a time delay term in the vibrators array model in Fig. 12. Consider the unit cells distributed in the *y*-axis are excited in sequence, their time delay can be described as:

$$\Delta t = (N-1)b\sin\alpha / c_0 \tag{24}$$

Adding the time delay term into Eq. (19), the received sound pressure in the far field due to a radiating cell *N* is:

$$p_N(\theta,\alpha,\omega,r) = \frac{a}{\sqrt{r}} e^{\{j\omega[t-(N-1)b\sin\alpha/c_0]-kr_N\}} \tag{25}$$

Following the derivation in Eq. (21), the total sound pressure field due to *N* grating elements with period *b* is:

$$p(\theta,\alpha,\omega,r) = \sum_1^N p_N(\theta,\alpha,\omega,r) = \frac{a}{\sqrt{r}} e^{(j\omega t-kr)} \frac{\sin[\frac{Nkb}{2}(\sin\theta+\sin\alpha)]}{\sin[\frac{kb}{2}(\sin\theta+\sin\alpha)]} \tag{26}$$

The directivity of sound radiation is changed to:

$$D(\theta,\alpha,\omega) = \left| \frac{\sin[\frac{Nkb}{2}(\sin\theta+\sin\alpha)]}{N\sin[\frac{kb}{2}(\sin\theta+\sin\alpha)]} \right| \tag{27}$$

Hence, the radiated sound power describing interference between unit cells can be described as:

$$W(\alpha,\omega) = \int_{\frac{-\pi}{2}}^{\frac{\pi}{2}} N^2 D(\theta,\alpha,\omega)^2 d\theta = \int_{\frac{-\pi}{2}}^{\frac{\pi}{2}} \left| \frac{\sin[\frac{Nkb}{2}(\sin\theta+\sin\alpha)]}{\sin[\frac{kb}{2}(\sin\theta+\sin\alpha)]} \right|^2 d\theta \tag{28}$$

Using the above equation, the frequency-dependent sound radiation intensity for five vibrators in two oblique cases ($\alpha = 20^\circ$ and 30°) are calculated and plotted in Fig. 17, where the separation distance is *d*=0.3 m (*b*=0.42 m). The two drops in the previous normal case (solid line in Fig. 13) are shifted towards lower frequencies due to the extra phase delay term as introduced in Eq. (28). Again, the interference induced variation in the radiation intensity curve is very significant. For example, at 650 Hz, the radiation intensity for the oblique case can be 5 dB stronger than the normal case.

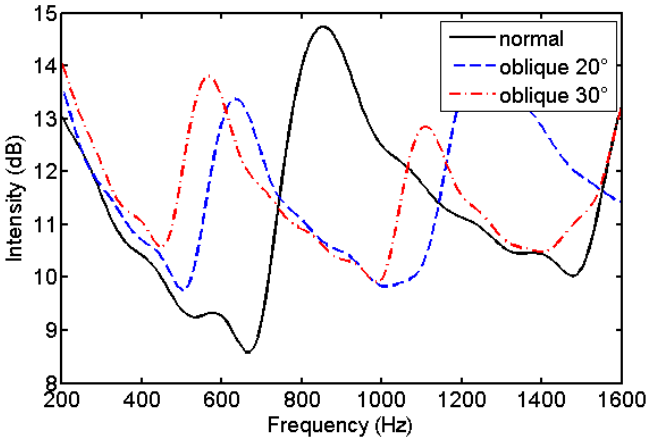

Fig. 17. Sound radiation intensity of five radiators in two oblique cases ($\alpha = 20^\circ$ and 30°), the separation distance is *d*= 0.3 m.

The STLs of acoustic gratings (comprising five unit cells, *d*=0.3 m) under normal and oblique incidences ($\alpha = 20^\circ$ and 30°) are compared in Fig. 18. For all three cases, the main STL peak due to the acoustic stop-band occurs at the same frequency (780 Hz), and the peak level is slightly weakened with oblique incidence. At other frequencies, the STL increment induced by interference among unit cells shifts to

lower frequency with a greater incidence angle, which follows the same trend as observed in Fig. 17. The STL dip induced by the diffraction effect, as explained previously in Sec. 4.1, basically remains at 500 Hz. These analyses conclude that the sound transmission through a metamaterial grating depends on the stop-band behavior of the unit cell (Sec. 3), the diffraction effect (Sec. 4.1) and the interference relationship (Sec. 4.2).

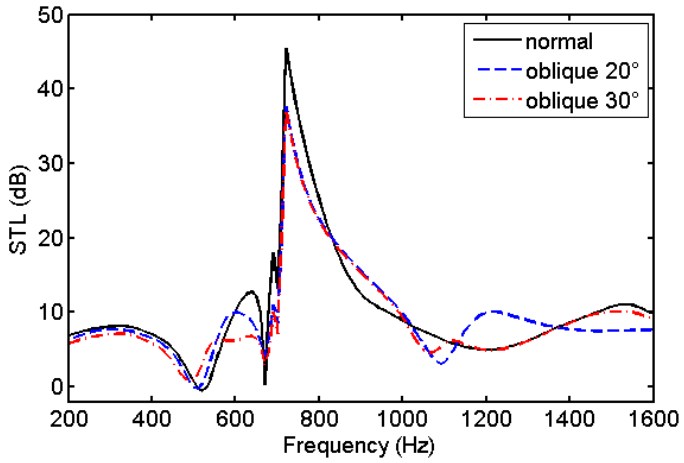

Fig. 18. STL of 5 cells acoustic grating under normal and oblique sound incidence.

5. Experimental validation

To validate the proposed numerical approach, an experimental test was performed using a two-dimensional acoustic plane as shown in Fig. 19. The height of the acoustic plane is set as 0.05 m. Five identical unit cells are closely connected together (d=0 m) to form an acoustic grating. Due to the size constraint, the experiment uses a 1:2 scale model, with the dimension of each unit cell in Fig. 6(a) being reduced by

half (to 0.06×0.06 m). The single-layer slab thus has a thickness of 0.06 m and a total length of 0.06× 5 =0.3 m. The sound source is a loudspeaker attached to a duct with a dimension of 0.9×0.3×0.05 m, which generates normal plane wave incidence to the slab. The duct is to facilitate an accurate measurement of the incidence sound power, although it may differ from the free-reflection condition assumed in simulations. At the receiving side, the outlet plane has a dimension of 1.2×0.94× 0.05 m, which is treated with acoustic wedges to minimize reflection. Three PCB array microphones (model 130E20) were used for measuring the sound pressure in the 2D plane. 'Mic.1' and 'Mic.2' were flush-mounted on the source duct to identify the incident and reflected sound wave, and 'Mic.3' is used to measure the outlet sound pressure along a semicircular path of radius 0.4 m. All the acquisition and control signals were controlled based on a NI PXI platform. The unit cells were fabricated using 3D printing technology on a Stratasys FORTUS 250MC printer with acrylonitrile butadiene styrene (ABS) additive. The wall thickness was set as 1 millimeter. The printed unit and the testing facility is shown in Fig. 20.

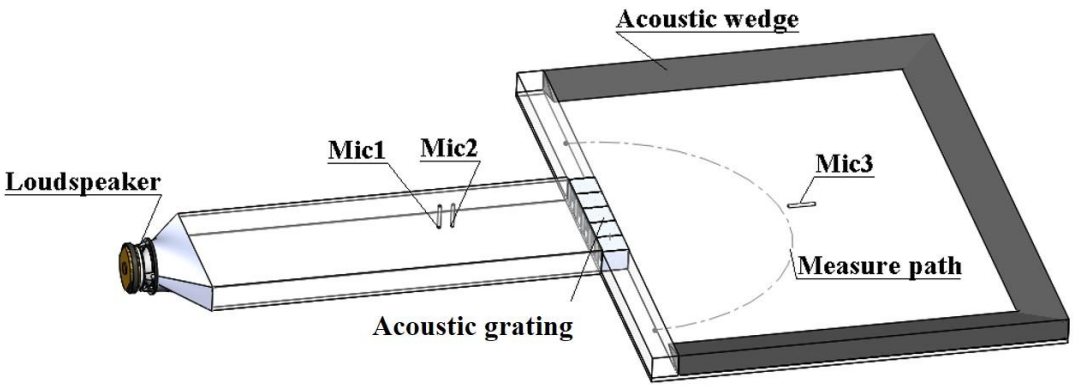

Fig. 19. Experimental set-up to measure the STL of an acoustic grating composed of periodic unit cells.

Figure 21 presents the predicted and measured STL for the constructed metamaterial acoustic grating from 400 Hz to 2800 Hz. Generally, a good agreement is observed between experiment and simulation, and high sound reduction close to 40 dB is experimentally captured at the stop-band frequency. The measured STL band over 10 dB is even wider than the prediction. This validates the proposed approach and shows the sound isolation capacity of the device. The discrepancies can be caused by a few plausible reasons such as the different sound incidence condition, geometric imperfection and experimental error. Future experiments will take these into account and improve the measurement accuracy.

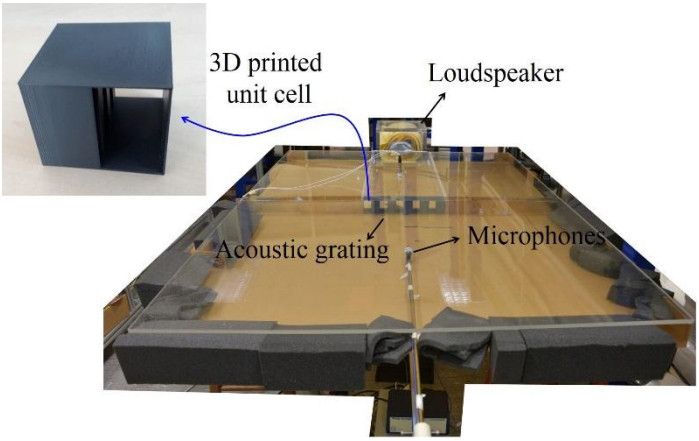

Fig. 20. Photo of the 3D printed unit cell and the experimental test-rig.

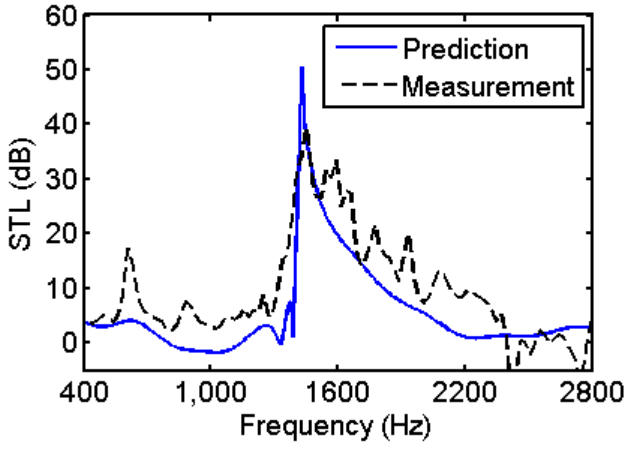

Fig. 21. Comparison between predicted and measured STL for the acoustic grating comprising 5 identical unit cells.

6. Conclusions

This paper has presented an investigation on the oblique sound transmission through an acoustic grating composed of sub-wavelength unit cells. The unit cell was constructed based on an acoustic duct decorated with space-coiled resonators, or, a duct-like metamaterial. A number of unit cells were arranged periodically in a slab to form an acoustic grating, aiming to provide both sound isolation and air ventilation in the design frequency range.

The metamaterial property of the unit cell has been analyzed using a simplified one-dimensional model (Sec. 3), showing negative effective material parameter and sub-wavelength character. Using the standard retrieval method, the obtained effective bulk modulus showed a negative region, which causes strong sound reflection. With multiple layers of resonators, the sound reflection was enhanced and broadened. A unit cell with three coiled resonators has a dimension of 0.12 m, which is about 0.27 of the wavelength at the stop-band frequency 780 Hz.

Using the developed numerical approach, the STL of the acoustic grating in a baffled condition has been analyzed. The mechanism study has uncovered three dominant effects that determine the STL curve, including the unit cell stop-band

property, diffraction effect and interference effect. Their effects can be summarized as follows:

1) The STL peak where sound transmission is strongly attenuated is attributed to the stop-band property of the unit cell. Baffled condition does not vary this frequency much compared to the one-dimensional condition. To obtain a slab structure with high sound isolation in a desired frequency range, the unit cell geometry can be optimized.
2) When the aperture size of the unit cell is smaller than the acoustic wavelength, especially at low frequency end, sound diffraction causes a unit cell to be acoustically transparent. At the diffraction frequency, the unit cell behaves like a duct-shaped aperture on the baffle.
3) Sound interference effect among the periodic unit cells changes the radiation pattern and varies the STL of the system. The interference relationship is frequency-dependent, which also depends on the grating period and sound incidence angle. A simplified model based on an array of point radiators was used to characterize such effect.

The validity of the proposed approach and numerical example was verified experimentally, which successfully captures high sound reduction capacity (close to 40 dB) in the experiment. This study indicates that sound transmission in an acoustic grating can be flexibly tuned or on-demand controlled by proper tuning of the geometry and periodicity of the grating elements. For such purpose, the physical aspects as detailed in this study could provide theoretical guidelines, and the proposed

numerical approach serves as an efficient design tool. Promising applications including ventilation windows or noise barriers for noise mitigation can be anticipated from this study. It is worth noting that the unit cells constituting the slab structure can be endowed with phase tailoring functionality to form an acoustic metasurface. The proposed modeling framework can be readily extended to metasurface studies.

References

[1] M.R. Haberman, M.D. Guild, Acoustic metamaterials, Physics Today, 69 (6) (2016) 42-48.

[2] G. Ma, P. Sheng, Acoustic metamaterials: From local resonances to broad horizons, Science Advances, 2 (2016) e1501595.

[3] S.A. Cummer, J. Christensen, A. Alù, Controlling sound with acoustic metamaterials, 1 (2016) 16001.

[4] Z. Liu, X. Zhang, Y. Mao, Y.Y. Zhu, Z. Yang, C.T. Chan, P. Sheng, Locally Resonant Sonic Materials, Science, 289 (5485) (2000) 1734-1736.

[5] Z. Yang, J. Mei, M. Yang, N.H. Chan, P. Sheng, Membrane-Type Acoustic Metamaterial with Negative Dynamic Mass, Physical Review Letters, 101 (20) (2008) 204301.

[6] N. Fang, D. Xi, J. Xu, M. Ambati, W. Srituravanich, C. Sun, X. Zhang, Ultrasonic metamaterials with negative modulus, Nat Mater, 5 (6) (2006) 452-456.

[7] M.S. Kushwaha, P. Halevi, L. Dobrzynski, B. Djafari-Rouhani, Acoustic band structure of periodic elastic composites, Physical Review Letters, 71 (13) (1993) 2022-2025.

[8] Y. Chen, G. Huang, X. Zhou, G. Hu, C.-T. Sun, Analytical coupled vibroacoustic modeling of membrane-type acoustic metamaterials: Membrane model, The Journal of the Acoustical Society of America, 136 (3) (2014) 969-979.

[9] F. Langfeldt, J. Riecken, W. Gleine, O. von Estorff, A membrane-type acoustic metamaterial with adjustable acoustic properties, Journal of Sound and Vibration, 373

(Supplement C) (2016) 1-18.

[10] F. Langfeldt, W. Gleine, O. von Estorff, Analytical model for low-frequency transmission loss calculation of membranes loaded with arbitrarily shaped masses, Journal of Sound and Vibration, 349 (Supplement C) (2015) 315-329.

[11] G. Ma, M. Yang, S. Xiao, Z. Yang, P. Sheng, Acoustic metasurface with hybrid resonances, Nat Mater, 13 (9) (2014) 873-878.

[12] Y. Cheng, C. Zhou, B.G. Yuan, D.J. Wu, Q. Wei, X.J. Liu, Ultra-sparse metasurface for high reflection of low-frequency sound based on artificial Mie resonances, Nat Mater, 14 (10) (2015) 1013-1019.

[13] X. Wu, C. Fu, X. Li, Y. Meng, Y. Gao, J. Tian, L. Wang, Y. Huang, Z. Yang, W. Wen, Low-frequency tunable acoustic absorber based on split tube resonators, Applied Physics Letters, 109 (4) (2016) 043501.

[14] Y. Xie, W. Wang, H. Chen, A. Konneker, B.-I. Popa, S.A. Cummer, Wavefront modulation and subwavelength diffractive acoustics with an acoustic metasurface, Nat Commun, 5 (2014).

[15] Y. Li, X. Jiang, R.-q. Li, B. Liang, X.-y. Zou, L.-l. Yin, J.-c. Cheng, Experimental Realization of Full Control of Reflected Waves with Subwavelength Acoustic Metasurfaces, Physical Review Applied, 2 (6) (2014) 064002.

[16] Y. Li, B. Assouar, Acoustic metasurface-based perfect absorber with deep subwavelength thickness, Applied Physics Letters, 108 (2016) 063502.

[17] V.M. García-Chocano, R. Graciá-Salgado, D. Torrent, F. Cervera, J. Sánchez-Dehesa, Quasi-two-dimensional acoustic metamaterial with negative bulk modulus,

Physical Review B, 85 (18) (2012) 184102.

[18] K.J.B. Lee, M.K. Jung, S.H. Lee, Highly tunable acoustic metamaterials based on a resonant tubular array, Physical Review B, 86 (18) (2012) 184302.

[19] N. Jiménez, V. Romero-García, V. Pagneux, J.-P. Groby, Quasiperfect absorption by subwavelength acoustic panels in transmission using accumulation of resonances due to slow sound, Physical Review B, 95 (1) (2017) 014205.

[20] N. Jiménez, V. Romero-García, V. Pagneux, J.-P. Groby, Rainbow-trapping absorbers: Broadband, perfect and asymmetric sound absorption by subwavelength panels for transmission problems, Scientific reports, 7 (2017) 13595.

[21] C. Wang, L. Huang, Y. Zhang, Oblique incidence sound absorption of parallel arrangement of multiple micro-perforated panel absorbers in a periodic pattern, Journal of Sound and Vibration, 333 (25) (2014) 6828-6842.

[22] P.R. Stepanishen, Acoustic two-dimensional radiation and scattering from cylinders using source density, SVD and Fourier methods, Journal of Sound and Vibration, 201 (3) (1997) 305-321.

[23] X. Yu, Z. Lu, L. Cheng, F. Cui, On the sound insulation of acoustic metasurface using a sub-structuring approach, Journal of Sound and Vibration, 401 (2017) 190-203.

[24] V. Fokin, M. Ambati, C. Sun, X. Zhang, Method for retrieving effective properties of locally resonant acoustic metamaterials, Physical Review B, 76 (14) (2007).

[25] D.R. Smith, S. Schultz, P. Markoš, C.M. Soukoulis, Determination of effective

permittivity and permeability of metamaterials from reflection and transmission coefficients, Physical Review B, 65 (19) (2002) 195104.

[26] M.C. Gomperts, T. Kihlman, The Sound Transmission Loss of Circular and Slit-Shaped Apertures in Walls, Acta Acustica united with Acustica, 18 (3) (1967) 144-150.

[27] D.J. Oldham, X. Zhao, Measurement of the sound transmission loss of circular and slit-shaped apertures in rigid walls of finite thickness by intensimetry, Journal of Sound and Vibration, 161 (1) (1993) 119-135.

Figure captions

Fig. 1. (a) A slab comprised of metamaterial unit cells arranged periodically to form a single-layer acoustic grating. Oblique sound incidence angle is defined relative to the slab normal; (b) The metamaterial unit cell is an open duct decorated with coiled resonators.

Fig. 2. Sound radiation from unit cell apertures into a semi-infinite free space.

Fig. 3. The real and imaginary part of self and mutual radiation impedance, aperture size h_o is 0.12 m, distance d_{nm} is 0.12 m.

Fig. 4. The effective bulk modulus calculated for a single unit cell with single coiled resonator layer, dimensions are given in cm.

Fig. 5. Transmittance of a unit cell with multiple layers of coiled resonators.

Fig. 6. (a) Unit cell geometry with three coiled resonators (in cm) and (b) the one-dimensional sound transmission loss.

Fig. 7. The four-pole parameters of the unit cell obtained using Eq. (9).

Fig. 8. STL of a single unit cell under normal or oblique sound incidence.

Fig. 9. Sound pressure field and intensity flow (represented by streamlines) at 500 Hz. Sound diffraction pattern in the incident field can be observed.

Fig. 10. The STL dips at 500 Hz and 1150 Hz match with the diffraction behavior in the sound transmission through a duct-like aperture.

Fig. 11. STL of an acoustic grating composed of five unit cells, with different separation distance, d = 0 m and d = 0.12 m.

Fig. 12. The aperture outlets of the periodic grating elements are simplified as an array of point radiators to explain the radiation interference effect.

Fig. 13. Sound radiation intensity of five radiators separated by different distances. Arrows denote radiation valley due to destructive interference.

Fig. 14. STLs of acoustic grating comprising 5 unit cells with different separation distance d.

Fig. 15. The radiation directivity predicted using Eq. (22) (polar plot) and the sound pressure distribution in the coupled system at 650 Hz, d=0.3m, normal incidence.

Fig. 16. The radiation directivity predicted using Eq. (22) (polar plot) and the sound pressure distribution in the coupled system at 1500 Hz, d=0.3 m, normal incidence.

Fig. 17. Sound radiation intensity of five radiators in two oblique cases ($\alpha = 20^\circ$ and 30°), the separation distance is d= 0.3 m.

Fig. 18. STL of 5 cells acoustic grating under normal and oblique sound incidence.

Fig. 19. Experimental set-up to measure the STL of an acoustic grating composed of periodic unit cells.

Fig. 20. Photo of the 3D printed unit cell and the experimental test-rig.

Fig. 21. Comparison between predicted and measured STL for the acoustic grating comprising 5 identical unit cells.

Figure 1a

Click here to download high resolution image

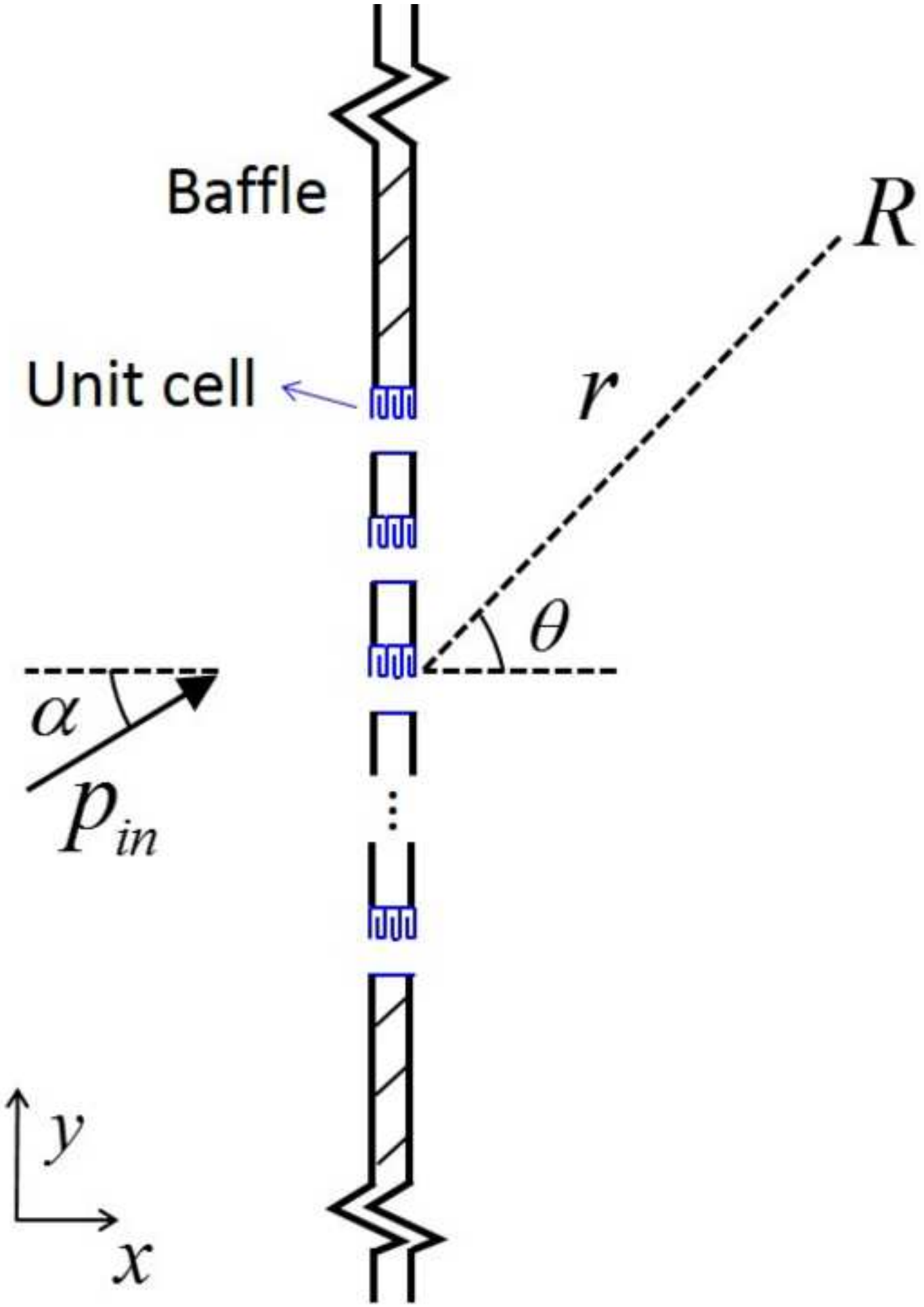

Figure 1b

Click here to download high resolution image

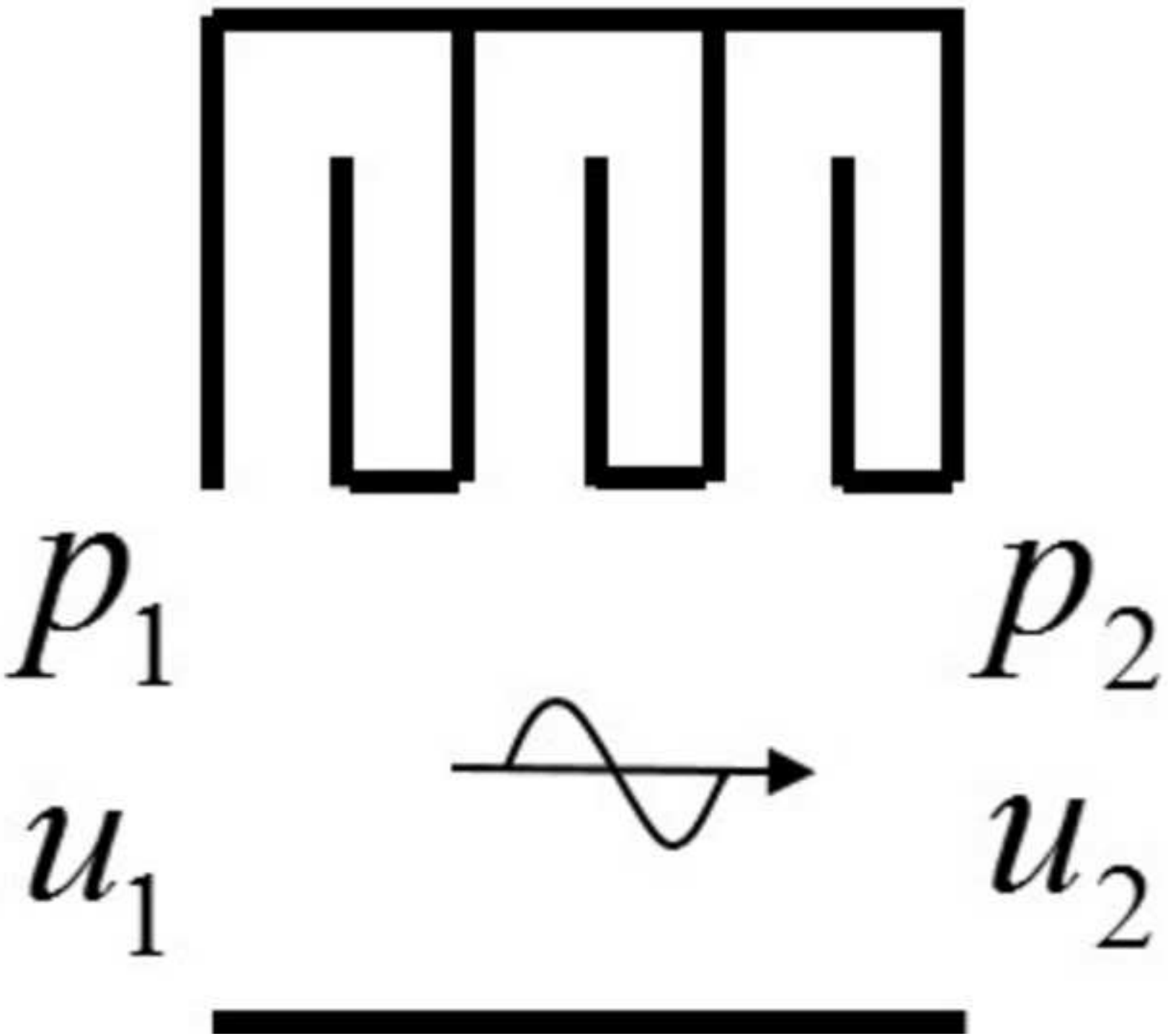

Figure 2

Click here to download high resolution image

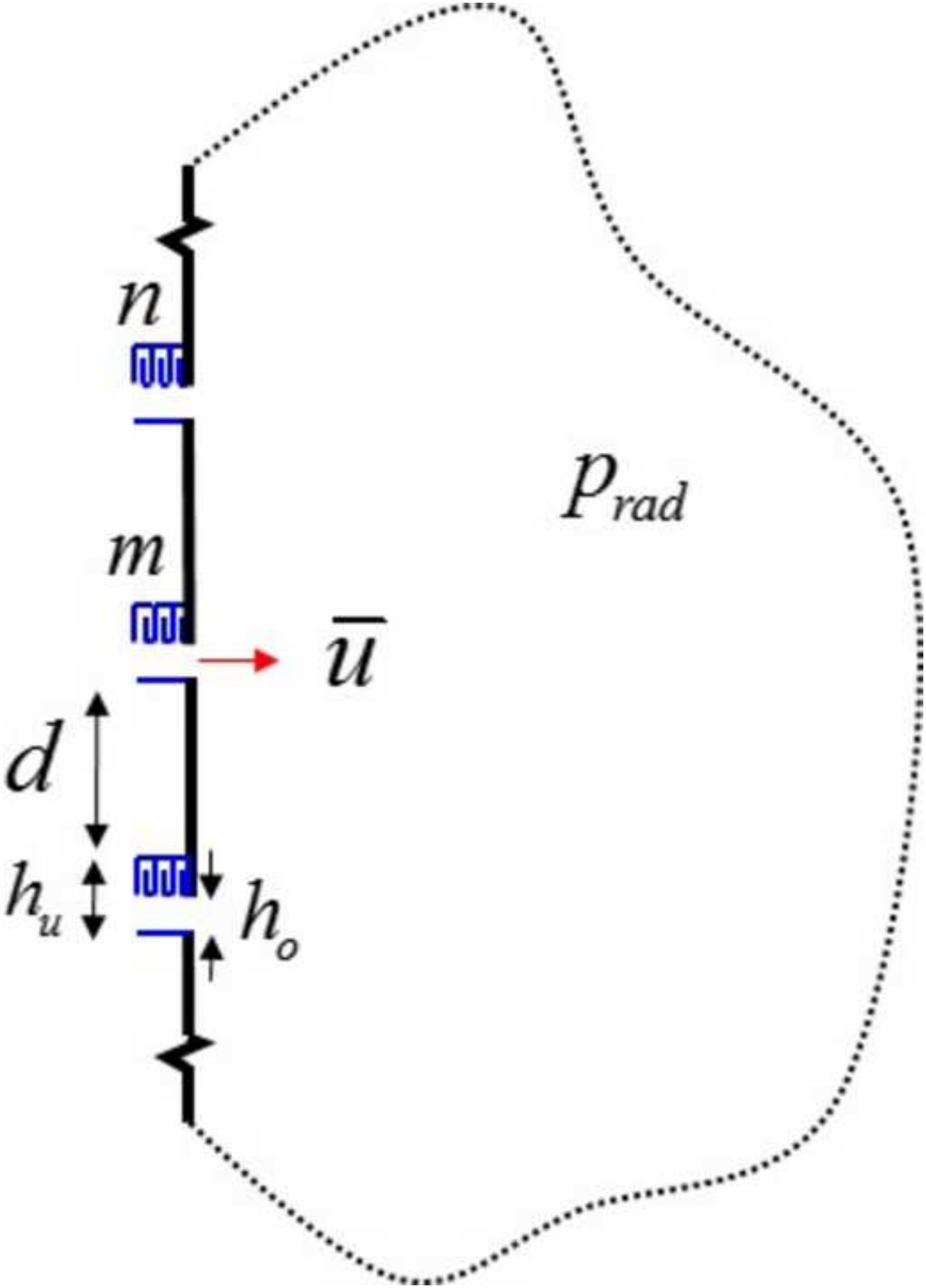

Figure 3

Click here to download high resolution image

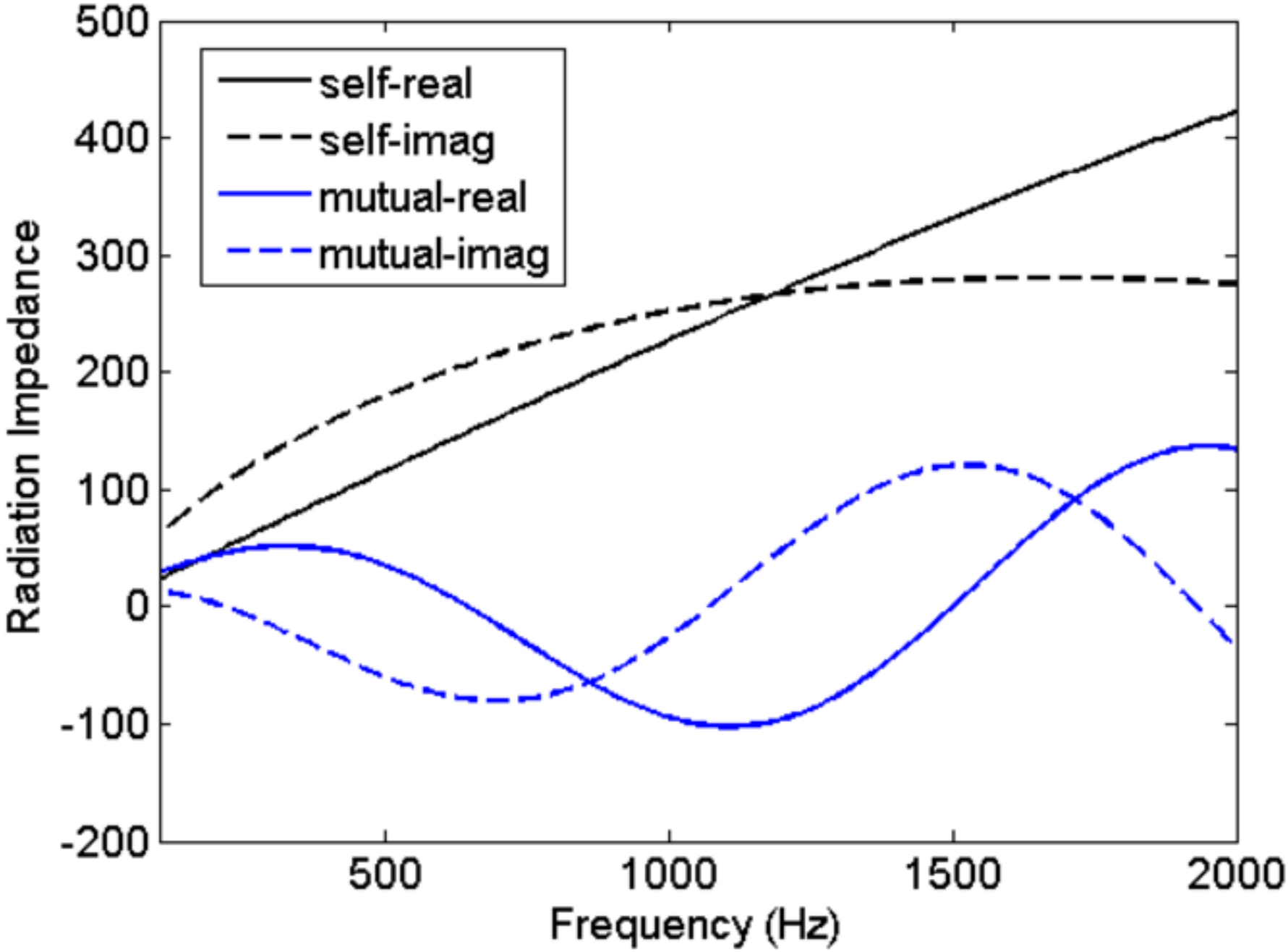

Figure 4

Click here to download high resolution image

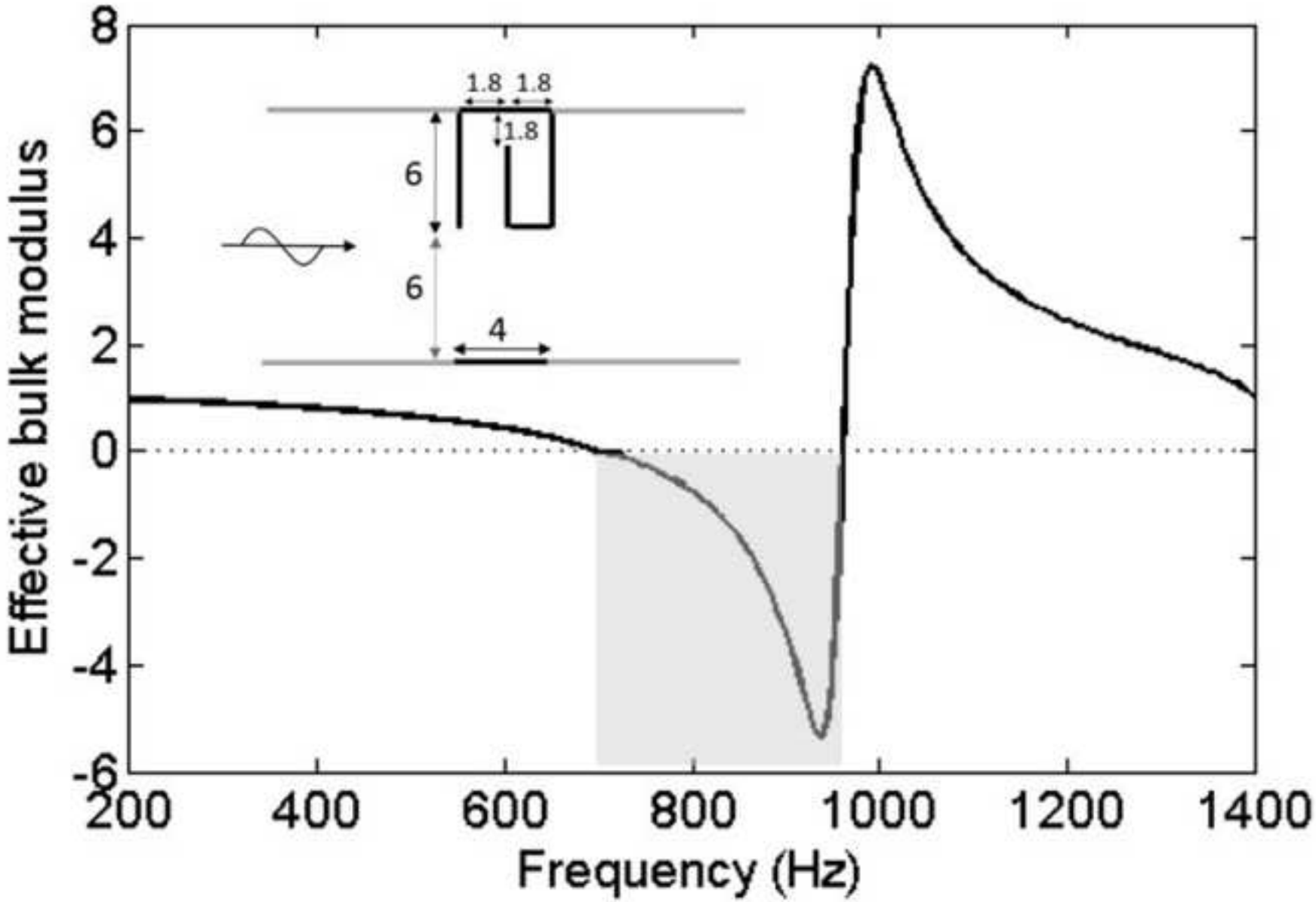

Figure 5

Click here to download high resolution image

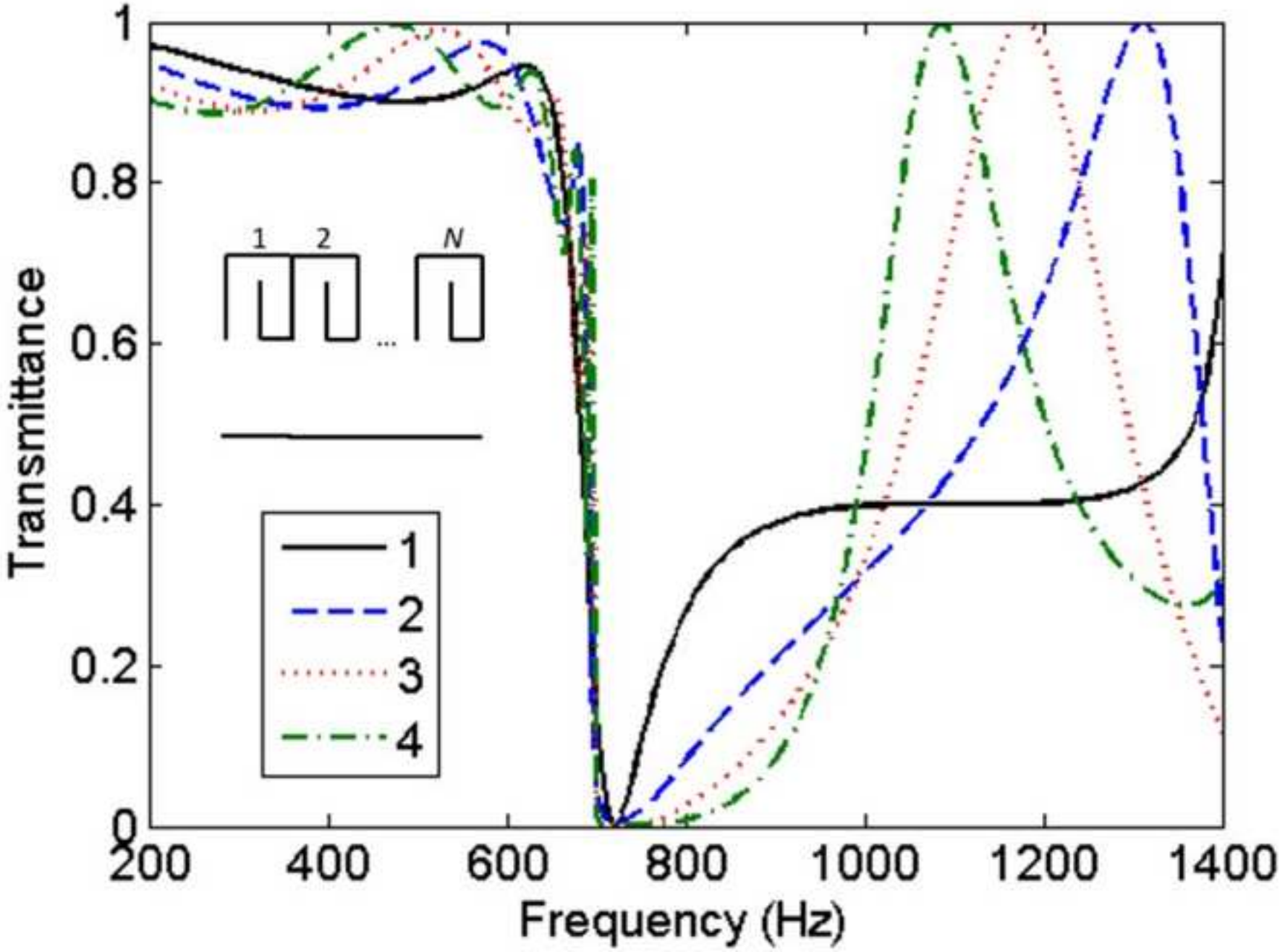

Figure 6

Click here to download high resolution image

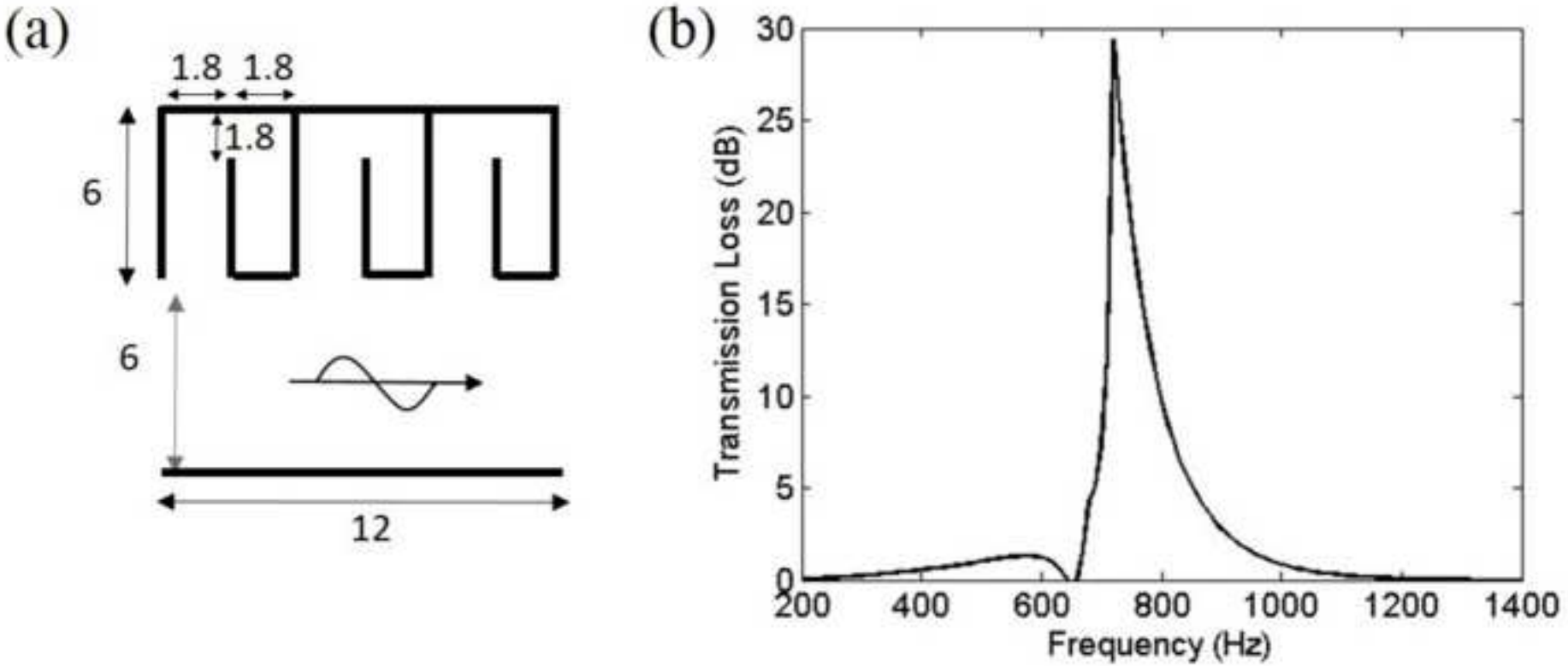

Figure 7

Click here to download high resolution image

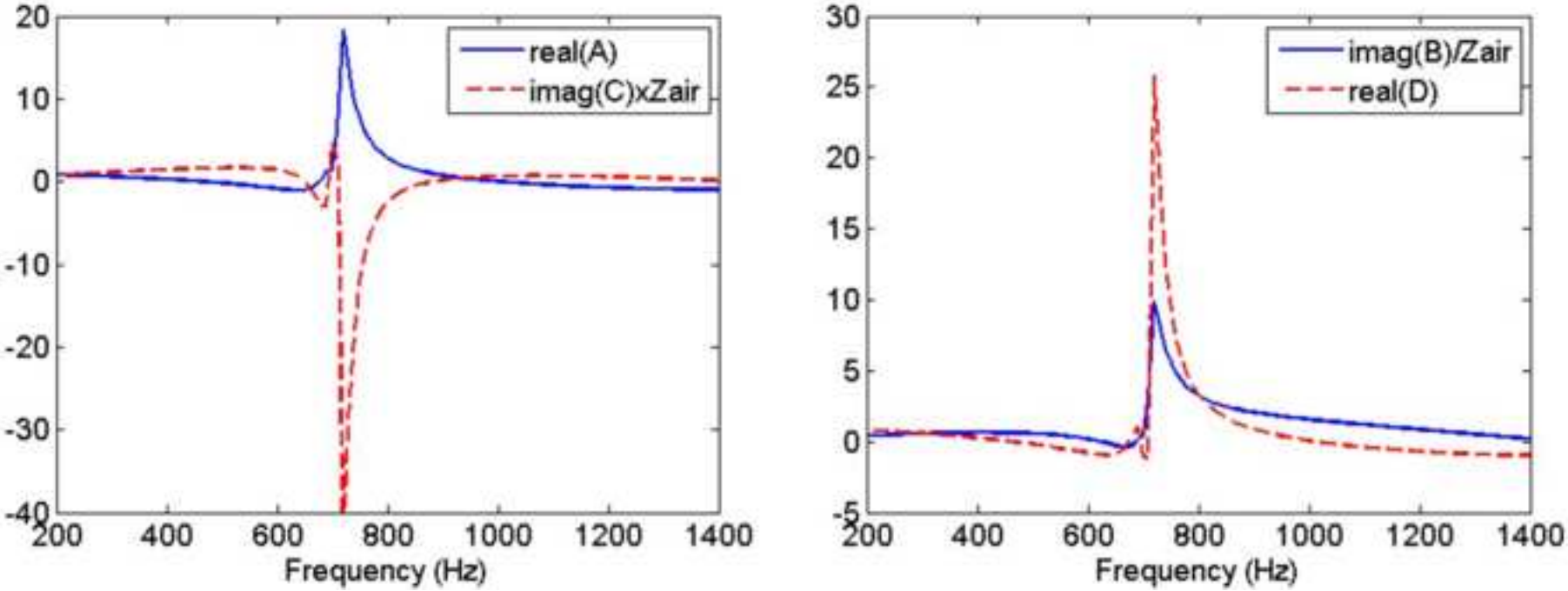

Figure 8

Click here to download high resolution image

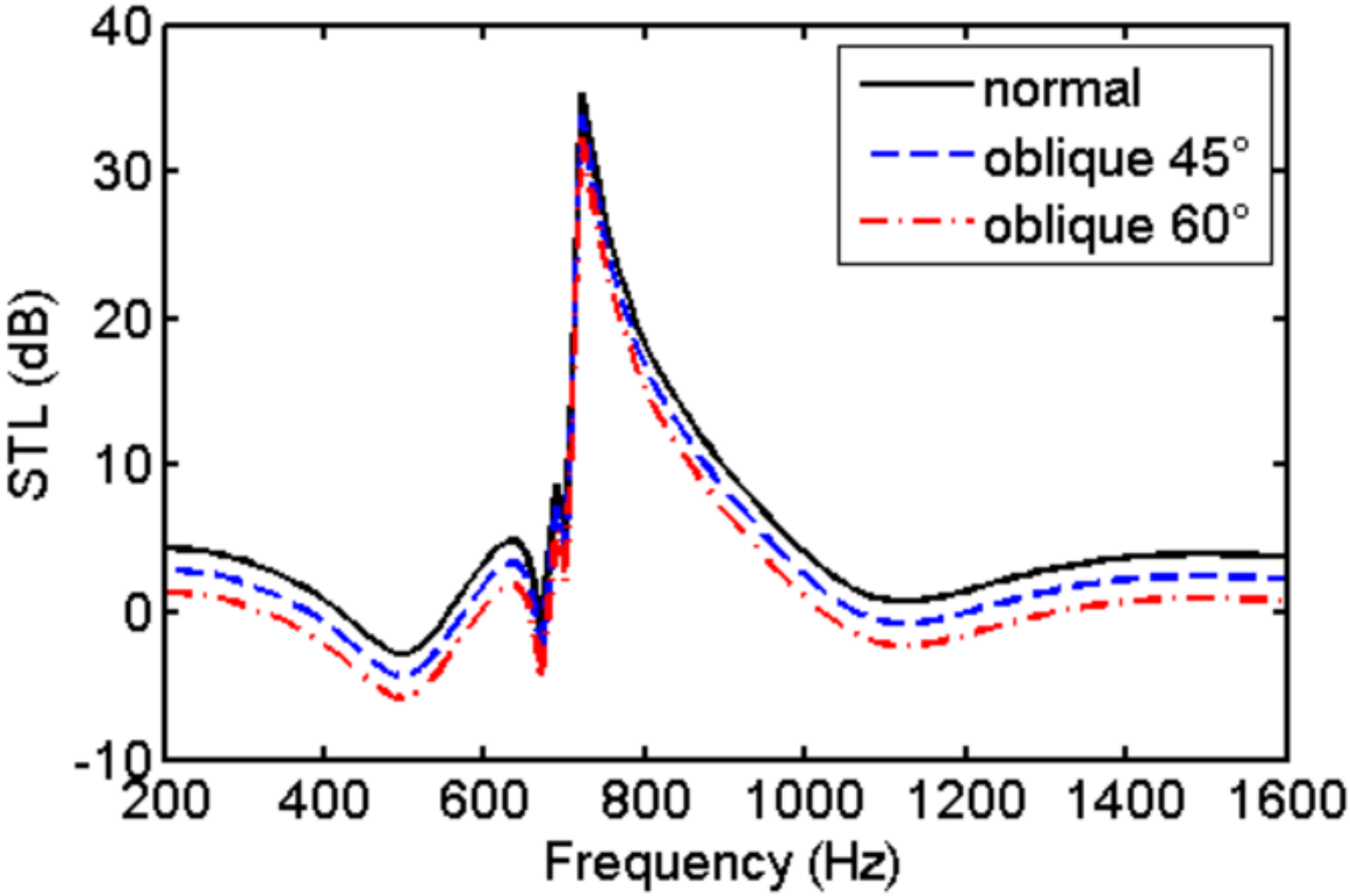

Figure 9

Click here to download high resolution image

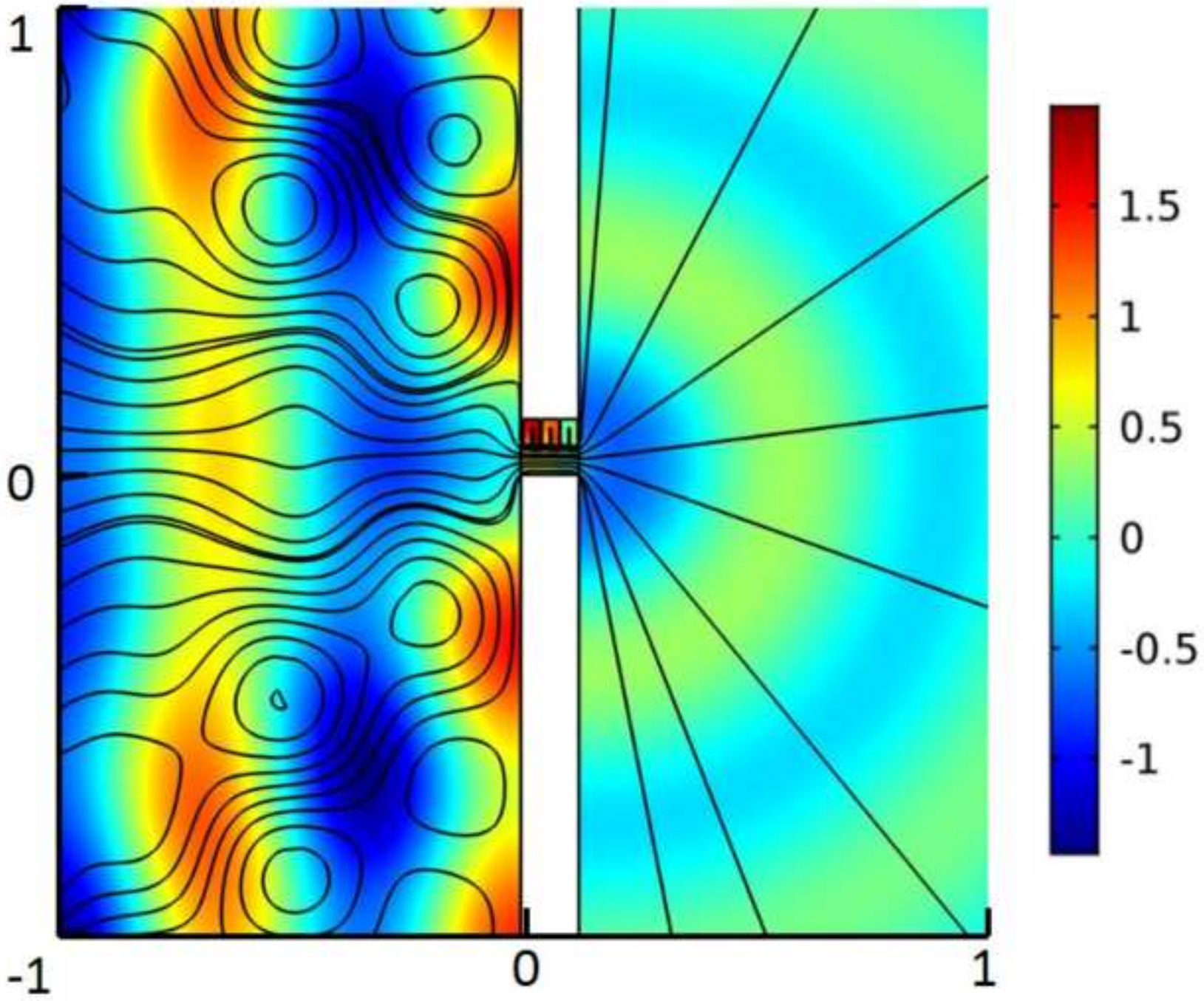

Figure 10

Click here to download high resolution image

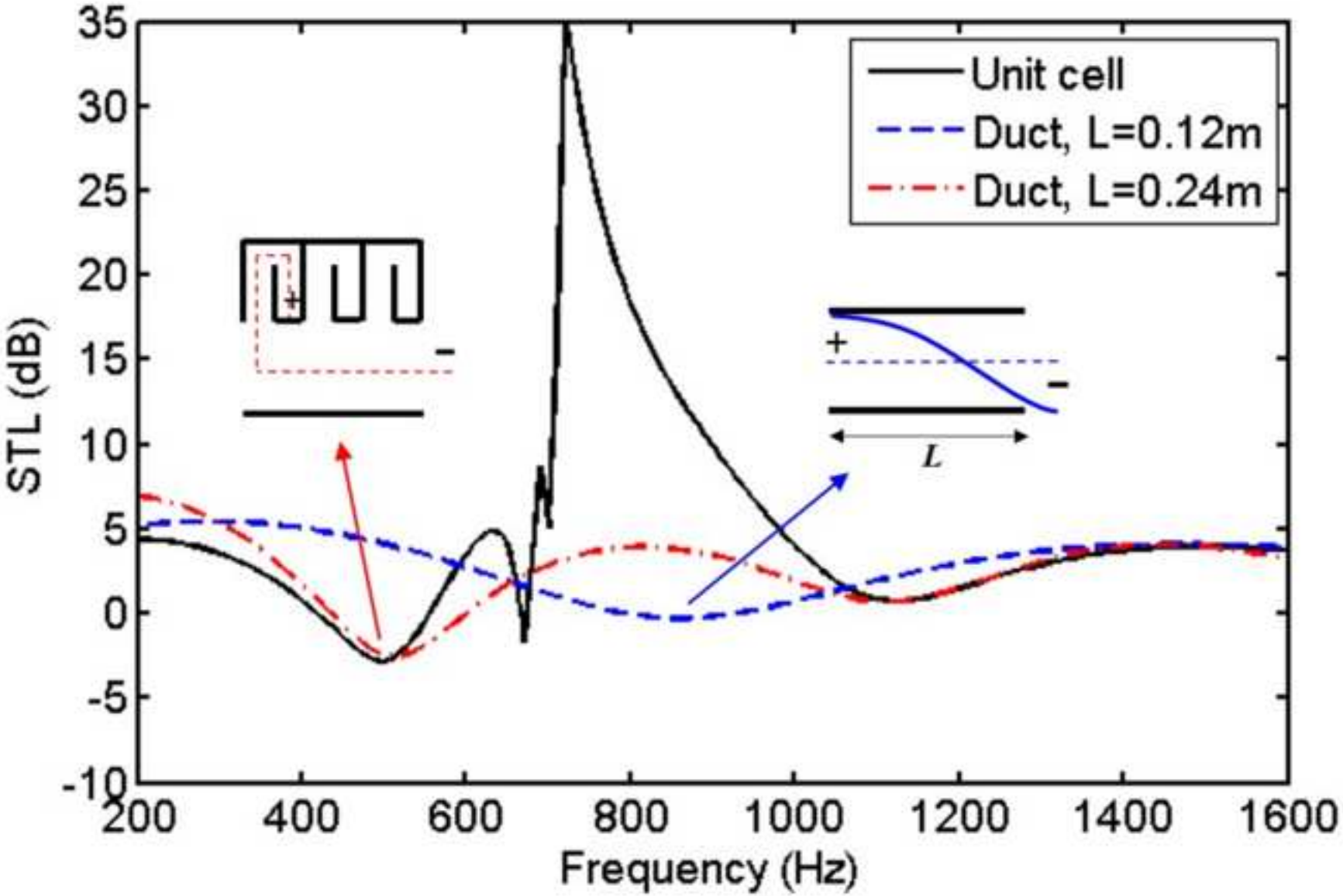

Figure 11
Click here to download high resolution image

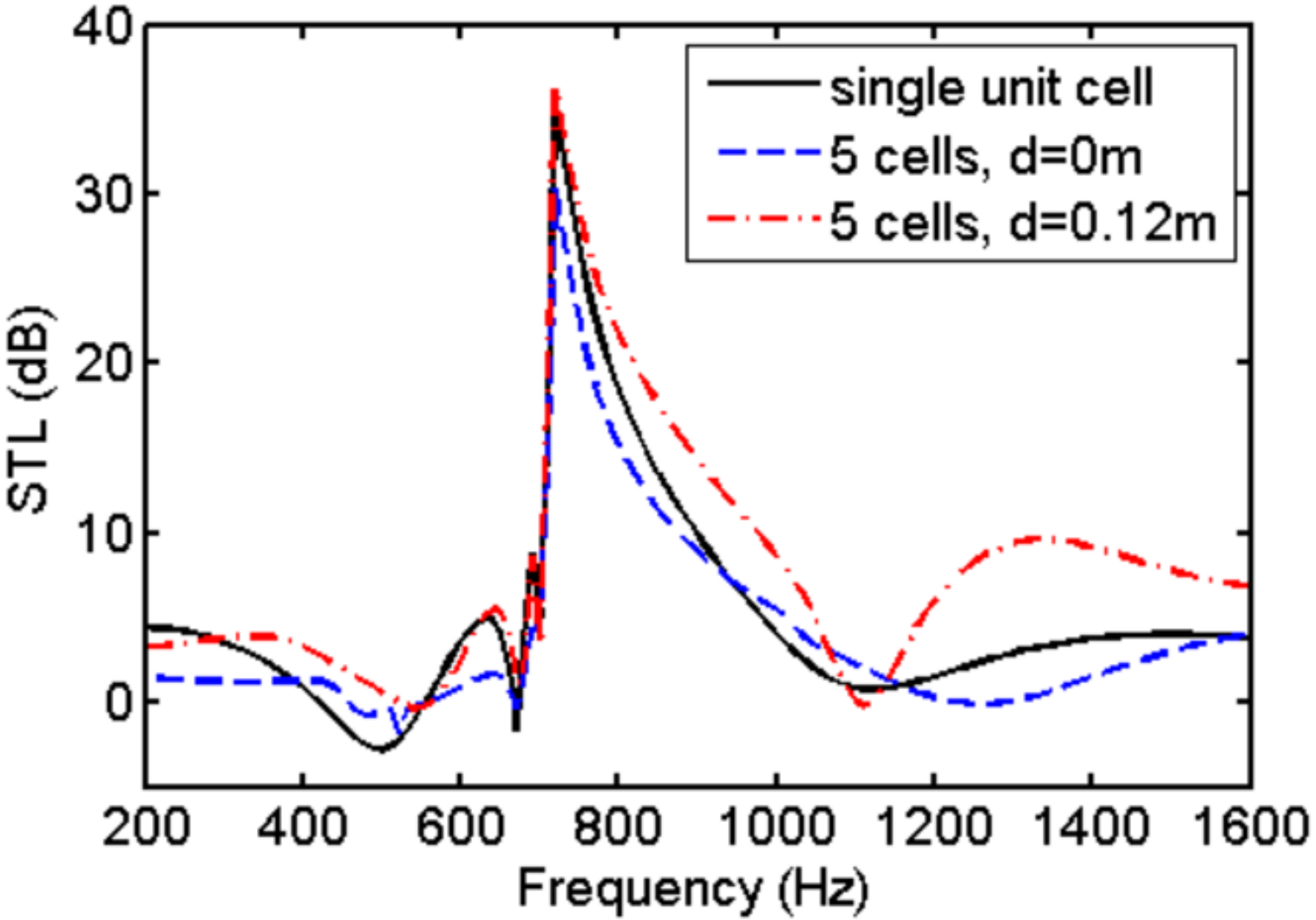

Figure 12
Click here to download high resolution image

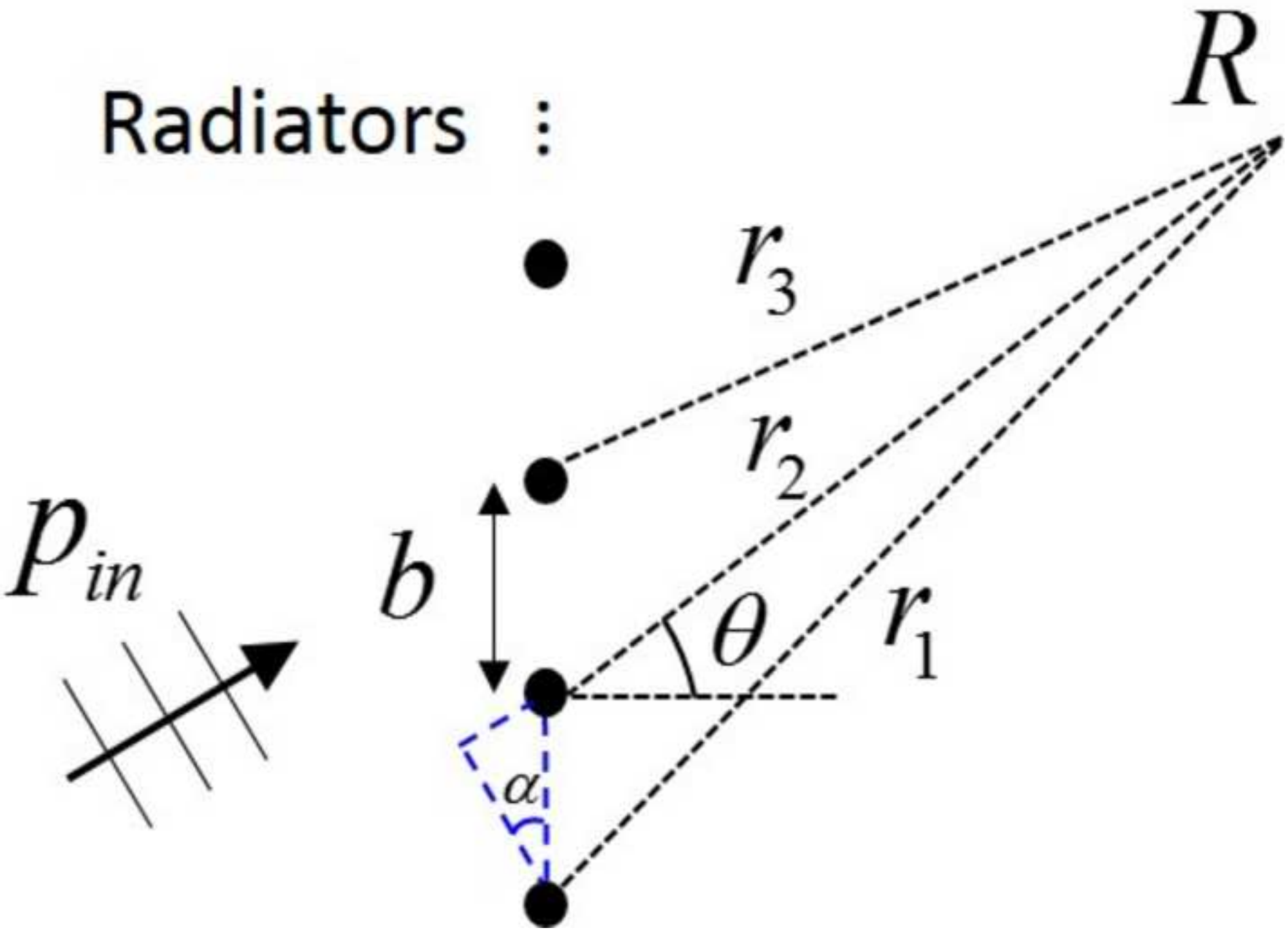

Figure 13
Click here to download high resolution image

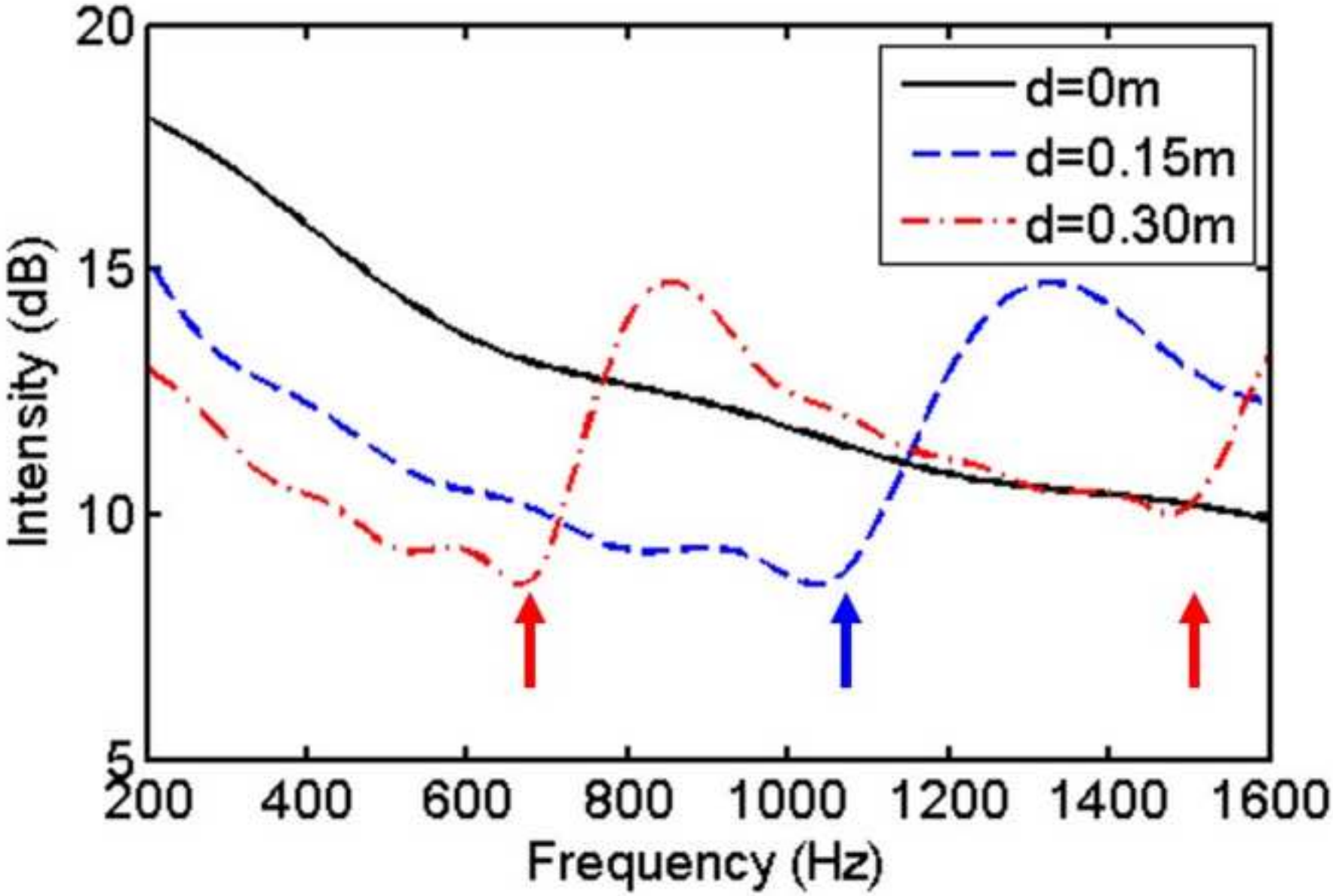

Figure 14
Click here to download high resolution image

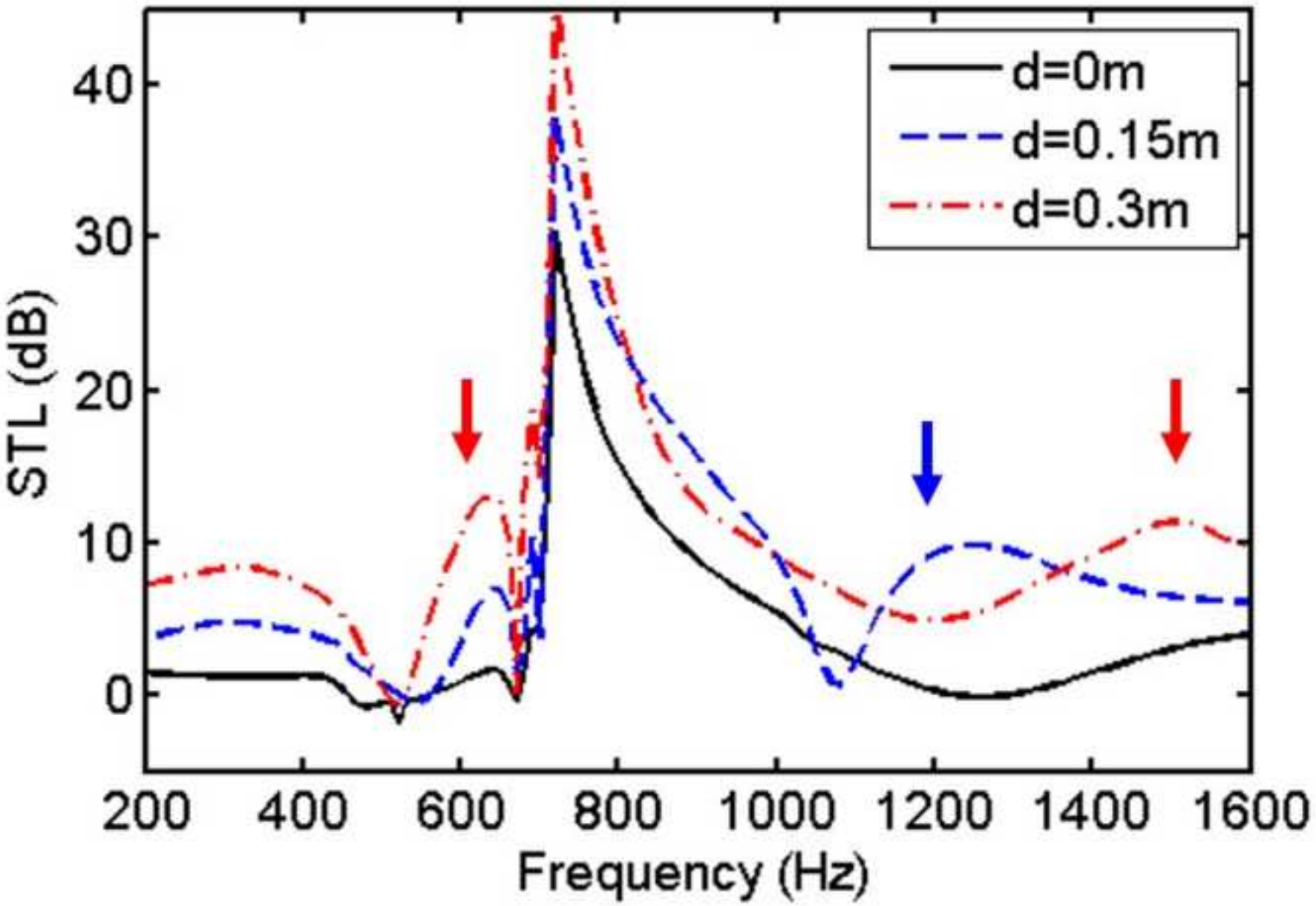

Figure 15

Click here to download high resolution image

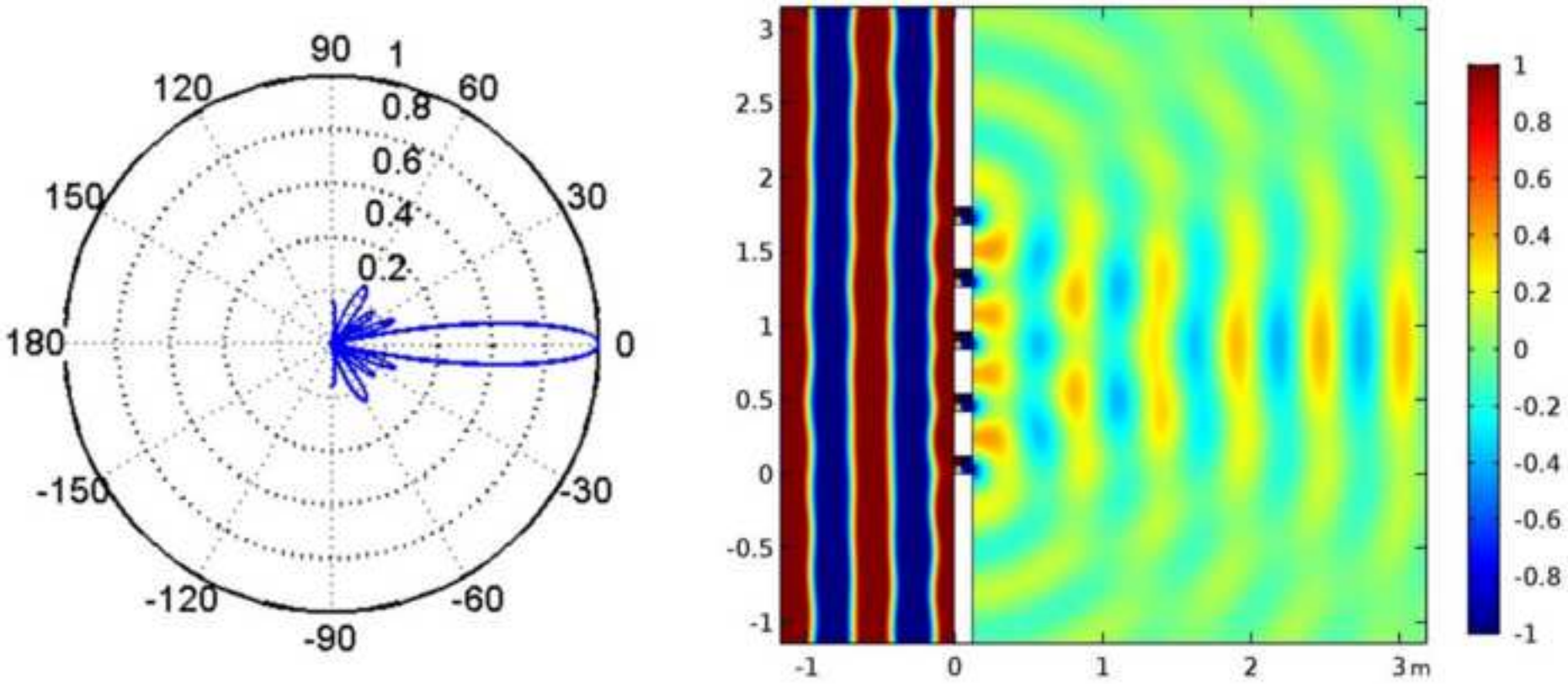

Figure 16

Click here to download high resolution image

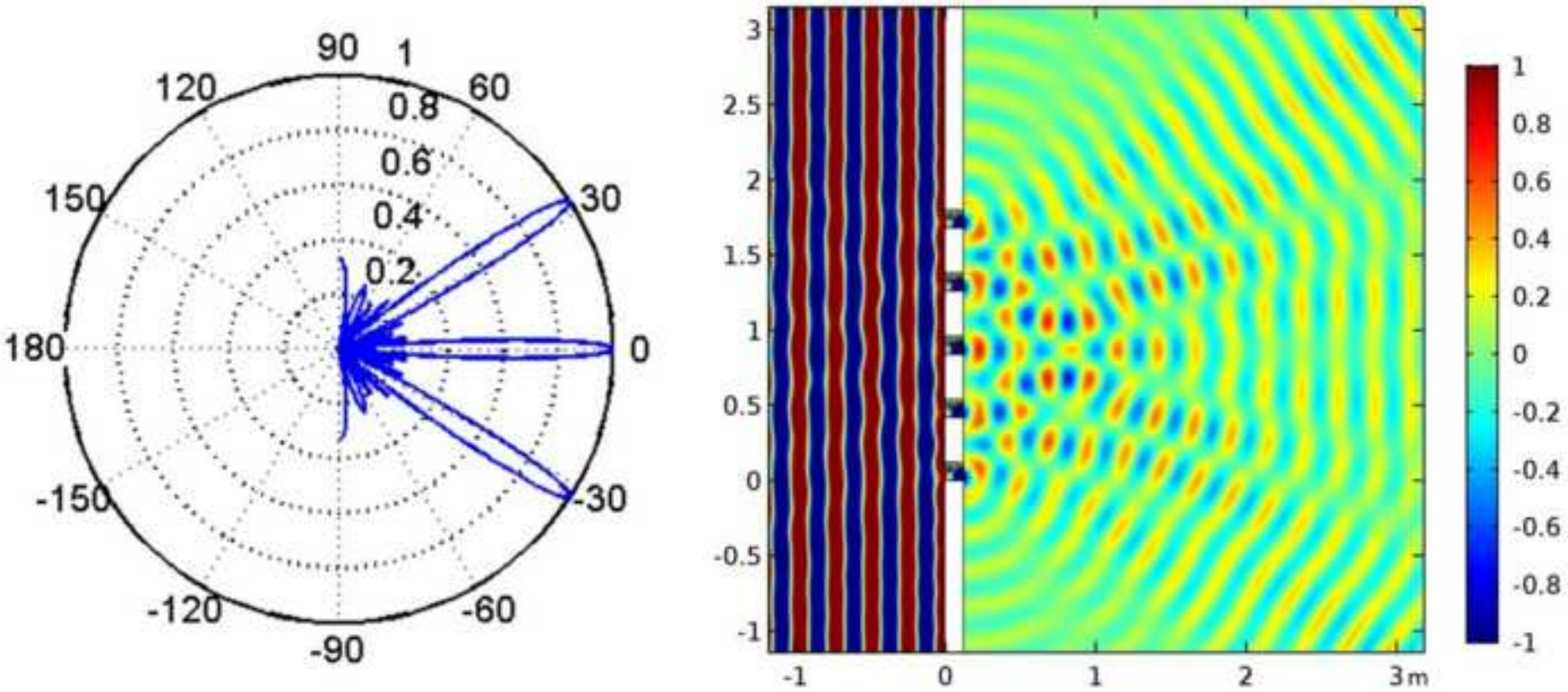

Figure 17
Click here to download high resolution image

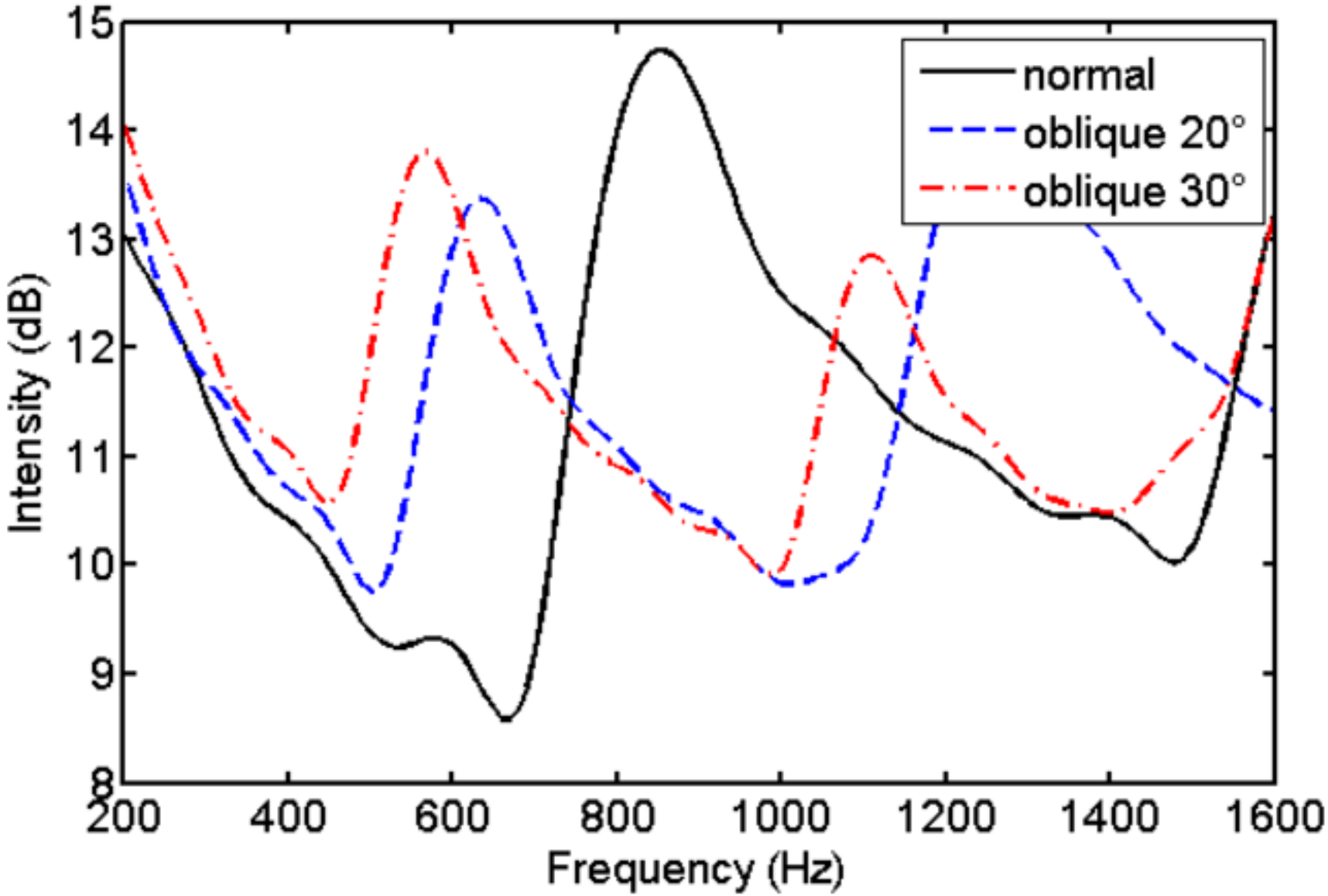

Figure 18

Click here to download high resolution image

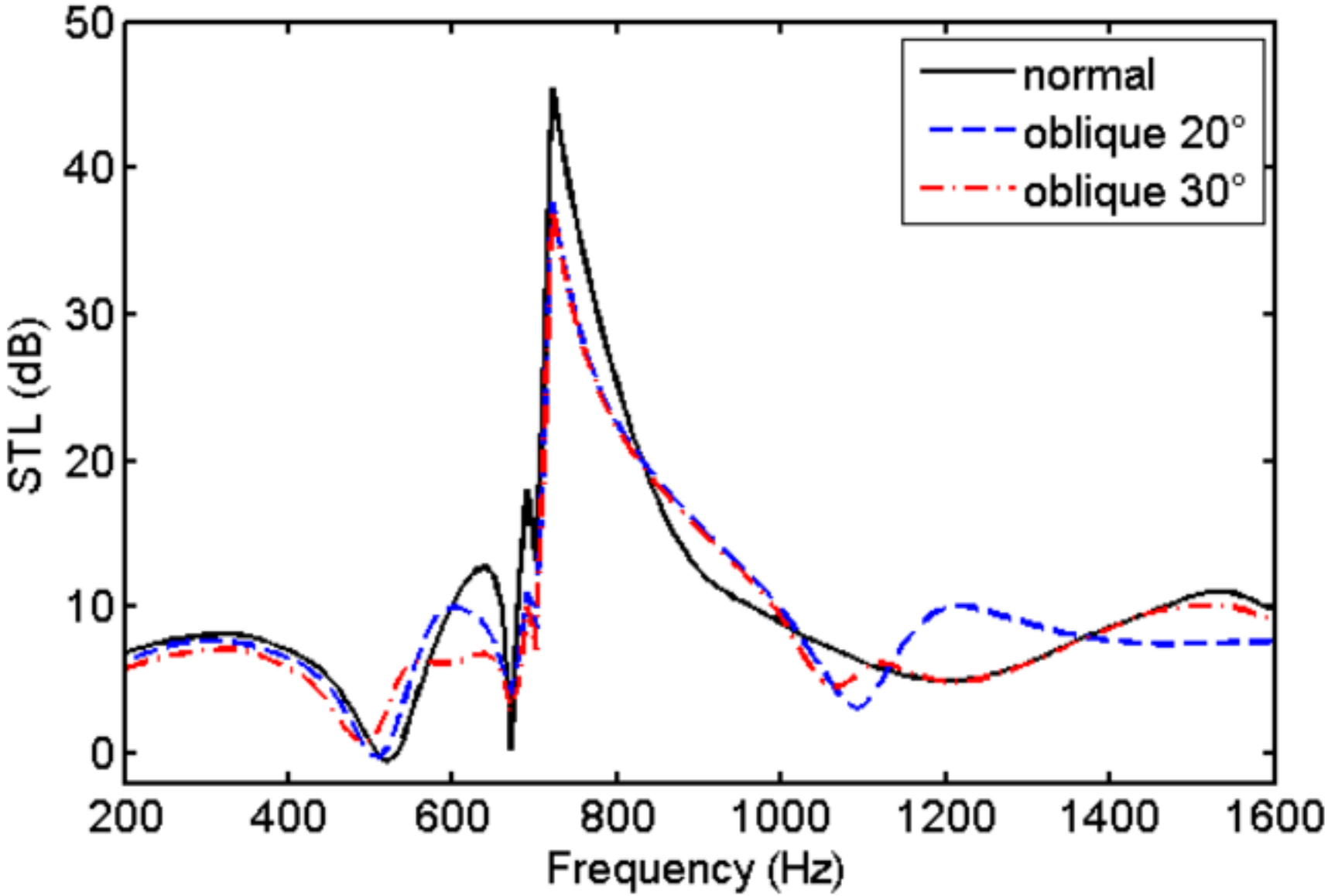

Figure 19
Click here to download high resolution image

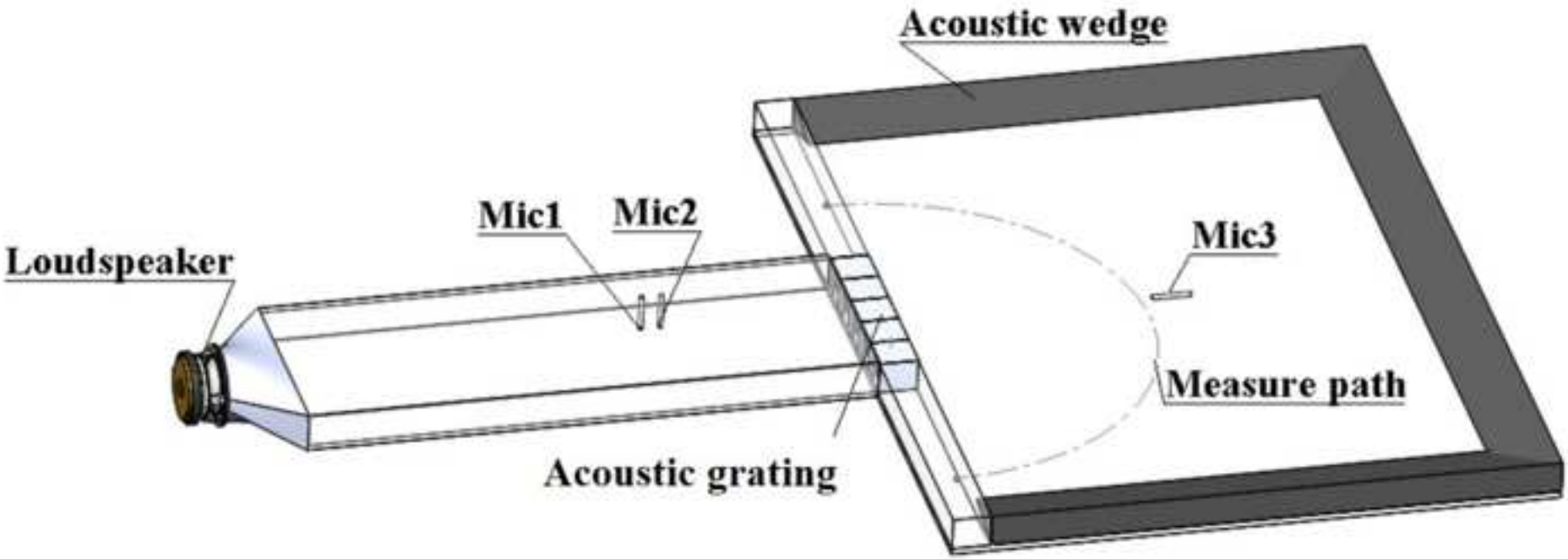

Figure 20

Click here to download high resolution image

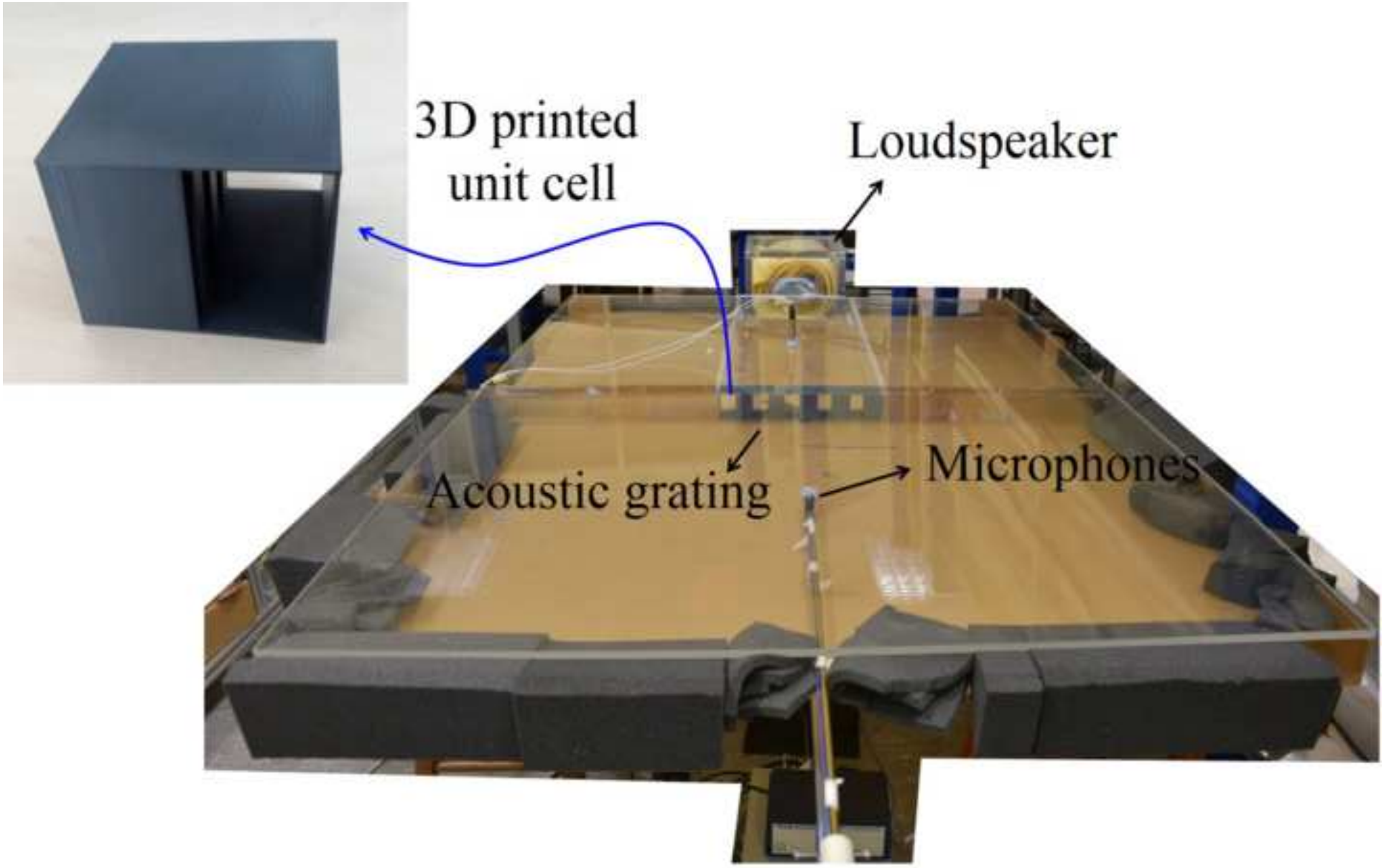

Figure 21
Click here to download high resolution image

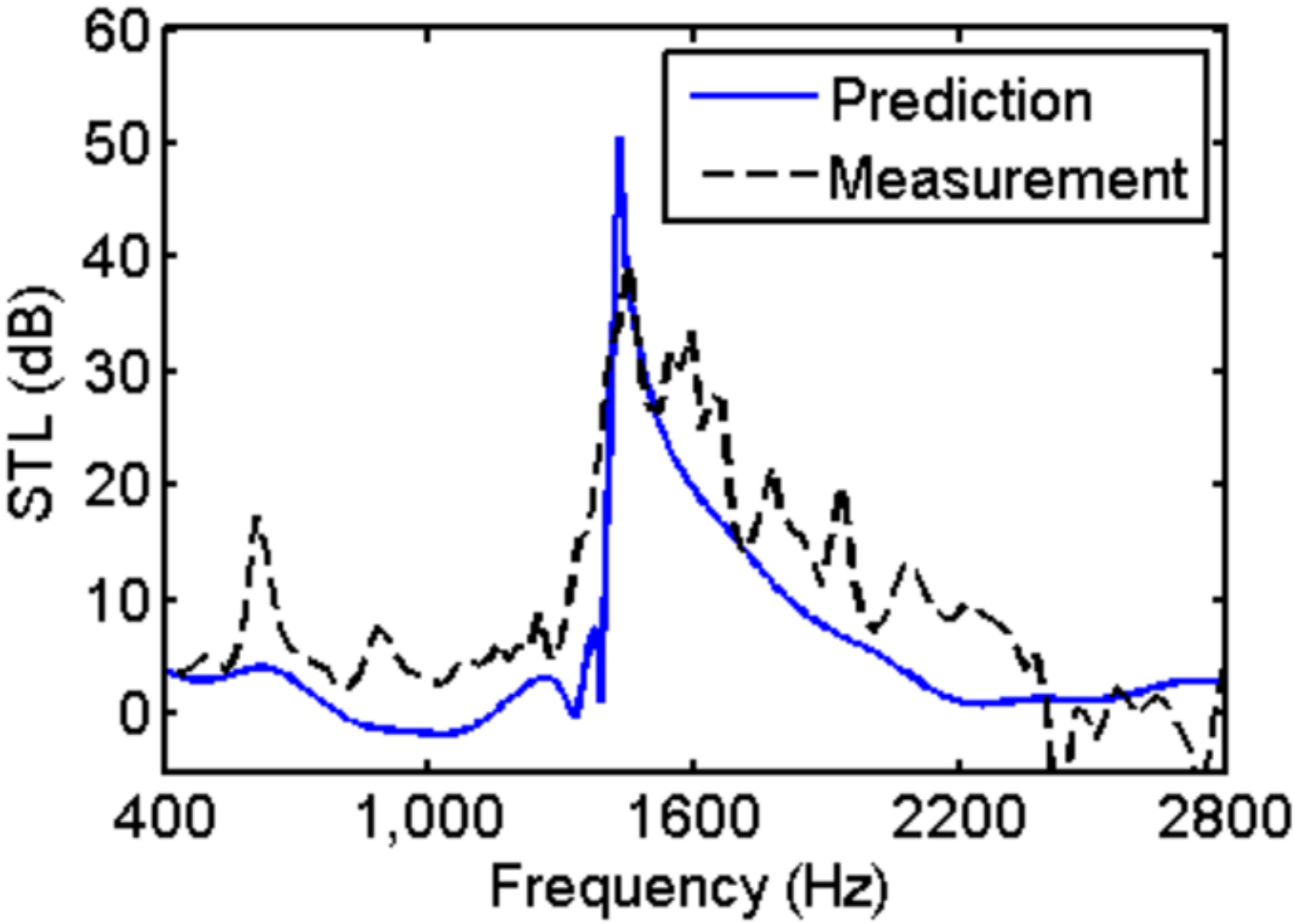

***Data Statement**

Click here to download Data Statement: dataprofile.xml